Modeling and Advanced Control of Dual Active Bridge DC-DC Converters

Shao, Shuai; Chen, Linglin; Shan, Zhenyu ; Gao, Fei; Chen, Hui; Sha, Deshang ; Dragicevic, Tomislav

Link back to DTU Orbit

Modeling and Advanced Control of Dual Active Bridge DC-DC Converters: A Review

Shuai Shao, *Member, IEEE*, Linglin Chen, Zhenyu Shan, *Member, IEEE*, Fei Gao, Hui Chen, Deshang Sha, *Senior Member, IEEE*, Tomislav Dragičević, *Senior Member, IEEE*

Abstract—The article classifies, describes and critically compares different modeling techniques and control methods for dual active bridge (DAB) dc-dc converters and provides explicit guidance about DAB controller design to practicing engineers and researchers. Firstly, available modeling methods for DAB including reduced order model, generalized average model and discrete-time model are classified and quantitatively compared using simulation results. Based on this comparison, recommendations for suitable DAB modeling method are given. Then we comprehensively review the available control methods including feedback-only control, linearization control, feedforward plus feedback, disturbance-observer-based control, feedforward current control, model predictive current control, sliding mode control and moving discretized control set model predictive control. Frequency responses of the closed-loop control-to-output and output impedance are selected as the metrics of the ability in voltage tracking and the load disturbance rejection performance. The frequency response plots of closed-loop control-to-output transfer function and output impedance of each control method are theoretically derived or swept using simulation software PLECS and MATLAB. Based on these plots, remarks on each control method are drawn. Some practical control issues for DAB including dead time effect, phase drift and dc magnetic flux bias are also reviewed. This paper is accompanied by PLECS simulation files of the reviewed control methods.

Index Terms—Dual active bridge (DAB), DC-DC, reduced order model, generalized average model and discrete-time model, feedback control, feedforward control, model predictive control.

I. INTRODUCTION

DC microgrids have higher efficiency, better current carrying capacity and faster dynamic response when compared to

Shuai Shao is with the College of Electrical Engineering and the Hangzhou Global Scientific and Technological Innovation Center, Zhejiang University, Hangzhou 310027, China (e-mail:shaos@zju.edu.cn).

Linglin Chen and Fei Gao are with the Department of Electrical Engineering, Shanghai Jiao Tong University, Shanghai 200240, China (e-mail:linglin.tim.chen@qq.com; fei.gao@sjtu.edu.cn).

Zhenyu Shan is with the School of Automation Science and Electrical Engineering, Beihang University, Beijing, China (e-mail: zhenyus@buaa.edu.cn).

Hui Chen is with the School of Information and Electrical Engineering, Zhejiang University City College, Hangzhou 310015, China (e-mail: chenh@zucc.edu.cn).

Deshang Sha is with the Advanced Power Conversion Center, School of Automation, Beijing Institute of Technology, Beijing 100081, China (e-mail: shadeshang@bit.edu.cn).

Tomislav Dragičević is with the Department of Electrical Engineering, Technical University of Denmark (DTU), Kongens Lyngby 2800 Kgs, Denmark (e-mail: tomdr@elektro.dtu.dk).
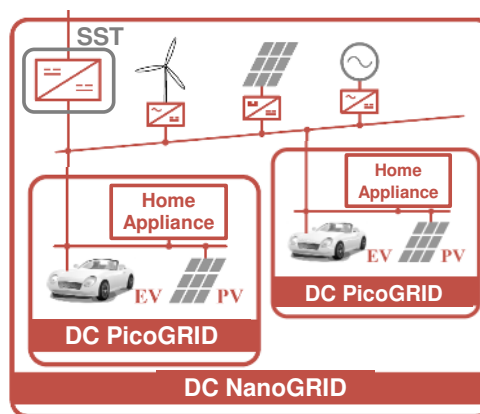

Fig. 1: Diagram of a hierarchical micro grid with SST as the energy router [2], [3].

conventional AC systems [1]. They also provide more natural interface with many types of renewable energy systems (RESs) and energy storage system (ESSs) and better compliance with consumer electronics [1]. These facts lead to increased applications of DC microgrid-type power architectures in remote households, data/telecom centers, renewable energy systems, electric vehicle charging stations, ships, aircrafts and others.

In DC microgrids, isolated bidirectional DC/DC (IBDC) power converters play an important role. IBDCs can serve as the interface of ESSs such as batteries and super capacitors to allow energy exchange between ESSs and the DC microgrid. They can also be stacked together to operate in the so-called solid-state transformer (SST) architecture, that can manage the power flow between DC microgrid and the upstream distribution network, as illustrated in Fig. 1.

Various IBDC topologies have been proposed, including bidirectional resonant converters, dual flyback, dual-Cuk, dual-push-pull, and dual active bridge (DAB) [4]. For the ESSs and micro-grids applications, the DAB (Fig. 2) originally proposed by de Doncker et al. [5] [6] is one of the most promising typologies for the following reasons [7]:

- Auto-adjust bidirectional power flow, ideal for SSTs and ESSs in micro-grids that often requires fast changes in power flow direction.
- Wide voltage conversion gain range, which is essential to interface ESSs such as batteries or super-capacitors, whose voltage can vary significantly under different states of charge.
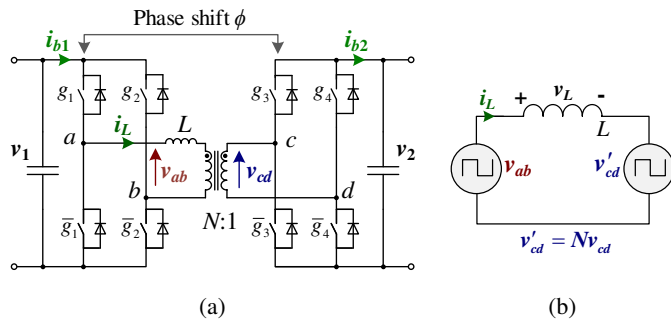- Zero voltage switching (ZVS) capability, able to achieve

Fig. 2: Topology of a DAB converter (a) and its equivalent circuit (b).

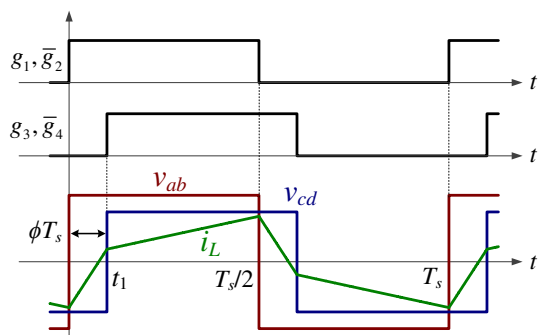high efficiency with proper control.

Fig. 3: Key waveforms of a DAB using SPS modulation.

Various applications employing DABs have been proposed. SSTs based on DABs in power grids have been introduced to interconnect different scale micro-grids [8] or to connect different levels of dc grids [9], [10]. Power electronic traction transformer (PETT) using DABs can reduce the weight, add additional functionalities and improve the energy efficiency compared to on-board line frequency transformer [11], [12]. DAB is also a promising solution for on-board battery chargers in plug-in electric vehicles (PEVs), especially when the vehicle-to-grid (V2G) function is required [13], [14]. With (gallium nitride) GaN devices, a 1MHz 1.2kW/400V DAB prototype is reported to achieve 97.5% peak efficiency [15]. With 1700V (silicon carbide) SiC devices, a 1500V/200kW DAB prototype is reported to achieve 99.6% peak efficiency [16], [17]. Other applications including ESS interface converters [18], airborne wind turbines [19], uninterrupted power supplies (UPS) [20], and power load emulators [21] have also been reported.

In all these applications, it is essential to model the DAB converter and design its controller with specified steady-state and dynamic performance. The aim of this paper is to classify, describe and critically compare different modeling techniques and control methods for DAB converters and provide explicit guidance about DAB controller design to practicing engineers and researchers. Section II categorizes the available modeling techniques for the DAB including reduced order model, generalized average model and discrete-time model. These models are quantitatively compared based on simulation results. Section III comprehensively describes

available control methods for DAB including feedback control, linearization control, feedforward plus feedback, disturbance-observer-based control, feedforward current control, model predictive current control, sliding mode control and moving discretized control set model predictive control (MDCS-MPC). The closed-loop control-to-output $G_{ro}(s)$ and output impedance $Z_o(s)$ are selected as the metrics of the ability in voltage tracking and the load disturbance rejection performance. The frequency response plots of $G_{ro}(s)$ and $Z_o(s)$ of each control method are theoretically derived or swept using simulation software. Based on these plots, remarks on each control method are drawn. Section IV reviews some practical control issues including dead time effect, phase drift and dc magnetic flux bias. Finally, Section V draws the conclusion.

Compared to the existing reviews about modeling and control [4], [7], [22], [23], this paper provides a more systematic overview of all known modeling and advanced control techniques for DAB. We are the first to quantitatively compare the available modeling methods and to recommend the most suitable models for controller design. Moreover, we also comprehensively describe the implementation of several advanced control methods and systematically evaluate these methods in frequency domain. We believe that such an approach provides valuable contribution to the field as it gives practicing engineers and researchers a clear guidance on how to: 1) Choose an appropriate modeling technique, 2) Choose which control method is the most suitable for their application , and 3) Understand how to formally analyze the performance of DAB converter in practice and implement its associated controller.

II. MODELING OF A DAB

Modeling is the representation of a physical phenomena by mathematical means [24]. DAB modeling is more challenging compared to modeling of conventional dc-dc converters as one of the state variables, the inductor current i_L, is purely ac with an average value 0, as shown in Fig. 3. This section summarizes modeling methods for a DAB converter, and compares the large and small signal models obtained from these methods using simulation results to give guidance for DAB controller design. The modeling methods are introduced based on a DAB using the single phase shift (SPS) modulation (Fig. 3), but these methods can be extended to a DAB using dual phase shift (DPS) or triple phase shift (TPS) modulation [7].

A. Reduced order model

One way to model DAB is simply ignoring the dynamics of i_L, which is called reduced order model [25]–[27]. The average values of input and output currents over one switching cycle (or half a cycle) are used to describe the characteristics of the current. Then a DAB is simplified to a first order system, as shown in Fig. 4, where $\langle i_{b1} \rangle$ and $\langle i_{b2} \rangle$ are the switching cycle average of the currents i_{b1} and i_{b2} (Fig. 2).

The output power P_o of a DAB modulated using SPS can be expressed as [6]

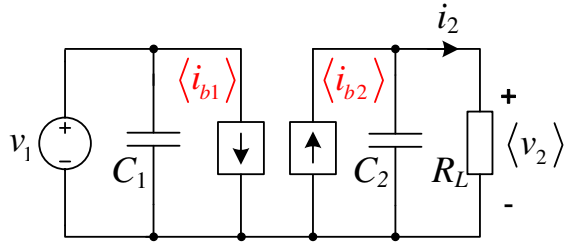$$P_o = \frac{N v_1 v_2 \phi (1 - 2|\phi|)}{f_s L} \tag{1}$$

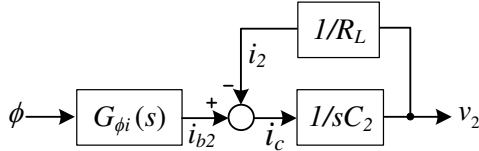Fig. 4: Large signal diagram of the DAB reduced order model [25]–[27].

Fig. 5: Block diagram of the reduced order model.

where N, v_1, v_2, ϕ, L are illustrated in Figs. 2 and 3, and f_s is the switching frequency of a DAB. Since $P_o = v_2 \langle i_{b2} \rangle$, $\langle i_{b2} \rangle$ can be calculated under positive power flow:

$$\langle i_{b2} \rangle = \frac{N v_1 \phi (1 - 2\phi)}{f_s L} \tag{2}$$

Introducing perturbation at phase shift, $\phi = \Phi + \hat{\phi}$, $\langle i_{b2} \rangle = I_{b2} + \hat{i}_{b2}$, we obtain the transfer function from ϕ to i_{b2}

$$G_{\phi i}(s) = \frac{\hat{i}_{b2}}{\hat{\phi}} = \frac{d\langle i_{b2} \rangle}{dt} = \frac{N V_1 (1 - 4\Phi)}{f_s L} \tag{3}$$

where V_1, V_2, Φ, I_{b2} are the quiescent values of v_1, v_2, ϕ, i_{b2}. Φ and I_{b2} can be expressed as

$$\Phi = \begin{cases} \dfrac{1}{4} - \sqrt{\dfrac{1}{16} - \dfrac{f_s L I_2}{2 N V_1}} & I_2 \geq 0 \\ -\dfrac{1}{4} + \sqrt{\dfrac{1}{16} + \dfrac{f_s L I_2}{2 N V_1}} & I_2 < 0 \end{cases} \tag{4}$$

$$I_{b2} = I_2 = V_2 / R_L \tag{5}$$

Based on Fig. 4 and (3), the control block diagram from ϕ to v_2 is shown in Fig. 5. The transfer function from ϕ to v_2 can be derived as:

$$G_{v\phi}(s) = \frac{\hat{v}_2}{\hat{\phi}} = \frac{N V_1 (1 - 4\Phi)}{f_s L} \frac{R_L}{R_L C_2 s + 1} \tag{6}$$

Based on the above analysis, the reduced order model of DAB is a first order system. For DAB modulated using DPS and TPS, the circuit model can also be represented using Figs. 4 and 5. The difference between the models of these methods is the gain $G_{\phi i}(s)$. It is more complex to compute this gain for DAB modulated using DPS or TPS, compared to DAB with SPS. The reduced order model for DAB with TPS is presented in [28]. Besides, it is possible to consider the parasitic parameters to slightly improve the reduced order model as shown in Fig. 6, where the parasitic parameters $(R_{eq}, R_{c1}, R_{c2}, L_{s1}, L_{s2})$ are indicated using red color [29]. The resultant model is more complex by considering these

insignificant parasitics. Actually, we will show in Section II.D that the reduced order model [Fig. 5] is accurate enough for the controller design.
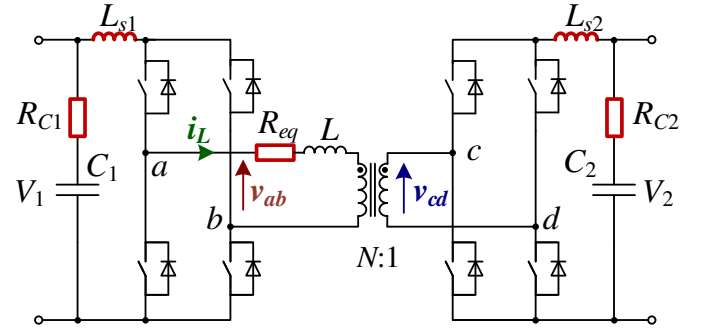

Fig. 6: DAB circuit considering the parasitic parameters.

B. Generalized average model

To include the dynamics of i_L, a generalized averaging technique can be applied to model the DAB. This averaging method is based on the representation of a signal $x(\tau)$ on the interval $\tau \in [t - T, t]$ by the Fourier series [30] [31] [32]

$$x(\tau) = \sum_{-\infty}^{\infty} \langle x \rangle_k (t) e^{jk\omega_s \tau} \tag{7}$$

where $\omega_s = 2\pi f_s$, and the complex number $\langle x \rangle_k (t)$ is the kth coefficient.
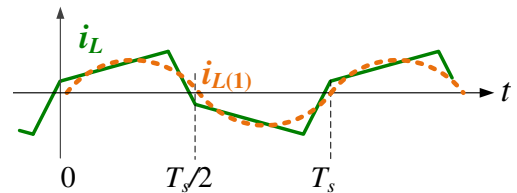
Fig. 7: Waveform of the inductor current i_L and its fundamental component $i_{L(1)}$.

Conventional state space averaging is a special case of the generalized average modeling method, in which only the dc term ($k = 0$) is considered. In the case of a DAB, the inductor current i_L is purely ac and it is natural to include more terms, and in [31] fundamental component of i_L ($k = \pm 1$, Fig. 7) and dc term of the output voltage (v_2) are considered. State space equation and small signal perturbation are employed to derive the small signal model [31]:

$$\begin{cases} d\mathbf{x}/dt = \mathbf{A}\mathbf{x} + \mathbf{B}\mathbf{U} \\ \mathbf{y} = \mathbf{C}\mathbf{x} \end{cases} \tag{8}$$

where $\mathbf{x} = \begin{bmatrix} \hat{v}_{2(0)} & \hat{i}_{LR(1)} & \hat{i}_{LI(1)} \end{bmatrix}^T$ and $\mathbf{y} = \begin{bmatrix} \hat{v}_{2(0)} \end{bmatrix}$. The subscripts "$R$" and "$I$" mean the real and imaginary parts of a complex number respectively, whereas the subscripts 0

and 1 mean the dc component and fundamental frequency component respectively. $\mathbf{A}$, $\mathbf{B}$, $\mathbf{C}$ are expressed as:

$$\mathbf{A} = \begin{bmatrix} -\dfrac{2}{R_L C_2} & -\dfrac{8N\sin(2\pi\Phi)}{\pi C_2} & \dfrac{-8N\cos(2\pi\Phi)}{\pi C_2} \\ \dfrac{4N\sin(2\pi\Phi)}{\pi L} & -\dfrac{2R_{eq}}{L} & 2\omega_s \\ \dfrac{4N\cos(2\pi\Phi)}{\pi L} & -2\omega_s & -\dfrac{2R_{eq}}{L} \end{bmatrix}$$

$$\mathbf{B} = \begin{bmatrix} \dfrac{8}{C_2}\left(I_{LI(1)}\sin(2\pi\Phi) - I_{LR(1)}\cos(2\pi\Phi)\right) \\ \dfrac{4V_{2(0)}}{L}\sin(2\pi\Phi) \\ -\dfrac{4V_{2(0)}}{L}\sin(2\pi\Phi) \end{bmatrix}$$

$$\mathbf{C} = \begin{bmatrix} 1 & 0 & 0 \end{bmatrix}^T$$

where $V_{2(0)}, I_{LI(1)}, I_{LR(1)}$ are the quiescent values of the state variables $v_{2(0)}, i_{LI(1)}, i_{LR(1)}$ respectively.

The transfer function from phase shift ϕ to output voltage v_2 can be derived below:

$$G_{v\phi}(s) = \mathbf{C}(s\mathbf{I} - \mathbf{A})^{-1}\mathbf{B} \qquad (9)$$

The resultant model can reflect the dynamics of i_L.

C. Discrete-time model

Same as the generalized average model, discrete-time model can include high frequency dynamics and is used for DAB modeling [33]–[37]. The discrete-time model views the state variables as only being changed at separate points of time. Consider a DAB modulating using SPS, there are four switching states in a switching cycle as shown in Fig. 8(a) and the state space equations can be obtained in each state as shown in Fig. 8(b). Then the state at $t = (k+1)T$, $\mathbf{x[k+1]}$, can be expressed using $\mathbf{x[k]}$:

$$\mathbf{x[k+1]} = \mathbf{Fx[k]} + \mathbf{GU[k]} \qquad (10)$$

where $\mathbf{x} = [i_L, v_2]^T$, $U = [v_1]$, the vector $\mathbf{F}$ and $\mathbf{G}$ can be calculated based on the state space equation and period of each state shown in Fig. 8, and were derived in [37].

The corresponding small-signal discrete-time model is obtained by introducing a phase perturbation $\hat{\phi}[k]$ around the steady-state time-varying vector $\mathbf{x[t]}$ as shown in Fig. 9 [35] [38]. Because the converter has two phase shift intervals per switching period, a phase perturbation alters the state at two points t_{p1} and t_{p2}, and the net results of phase perturbation at these two points are $\hat{x}_{d1}$ and $\hat{x}_{d2}$, as shown in Fig. 9. The instantaneous state perturbations are propagated to the end of the switching period through χ_1 and χ_2, which are calculated in [35]. The small signal model can be derived accordingly.

Using discrete-time modeling method, very accurate models can be obtained for high frequency or digitally controlled converters. This method can easily consider the ZVS transition, as well as the sampling, modulator effects and delays in the digitally control loop. The drawback of the discrete-time model is the complex calculation due to the product of matrix exponentials. This is especially the case for a DAB
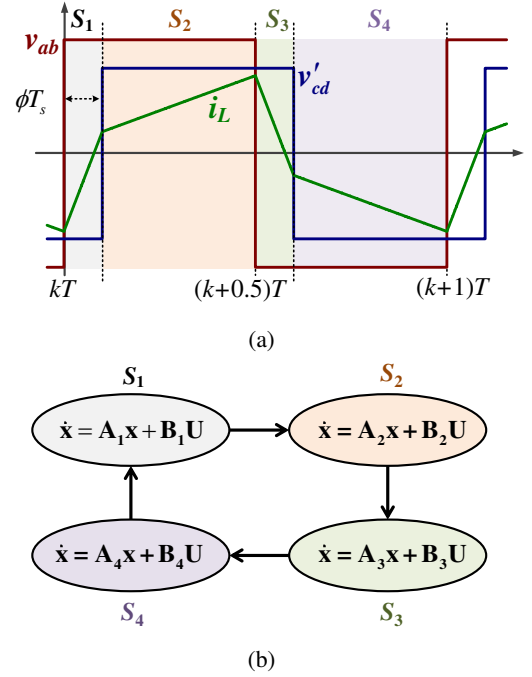

(a)

(b)

Fig. 8: Discrete-time modeling for a DAB, (a) states definition, (b) state space equation in each state.
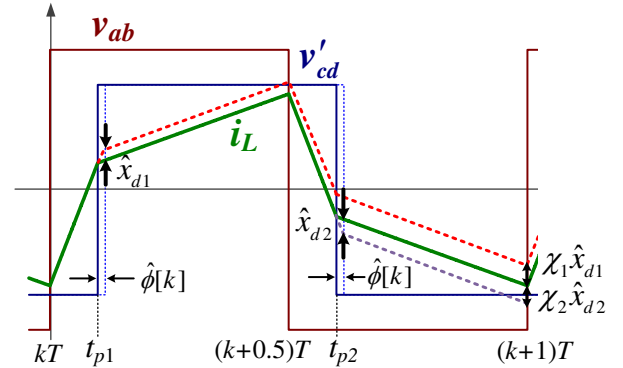
Fig. 9: Small signal modeling based on discrete-time model.

since there are at least four states in each switching cycle [35]. To simplify the calculation, the matrix exponential can be simplified by its bilinear Taylor series, $e^{\mathbf{A}_i t_i} \approx \mathbf{I} + \mathbf{A}_i t_i$ or through a modified bilinear expansion [33] [36] [37]. Still, the calculation of discrete method is much more complex than that of the continuous ones, and softwares such as MATLAB are required to complete the calculation.

D. Comparison of different DAB modeling methods

The four different DAB models: reduced order model [25], [26], improved reduced order model [29], generalized average model [31] and discrete-time model [35], [37], are compared with simulation results. The comparisons are based on a DAB with parameters listed in Table I, an equivalent resistor R_{eq} is included to represent the power losses caused by power devices and transformers as shown in Fig. 10. A dead time 200ns is considered in the simulation.

TABLE I: DAB circuit parameters used for model comparison.

		Nominal value[a]
N	Transformer turns ratio	2:1
f_s	Switching frequency	20kHz
L	Inductance	$L_0 = 70\mu H$
R_{eq}	Equivalent resistance	$R_{eq0} = 0.25\Omega$
C_2	DC Capacitor 2	$C_{20} = 1mF$
R	Load resistor	4Ω
T_d	Dead time	200ns

a: The nominal value is the value used in the DAB circuit. The circuit parameters used in the control can be different from this nominal value.
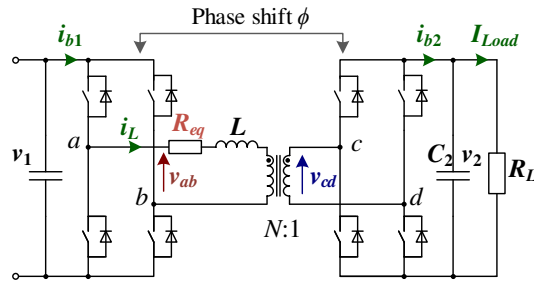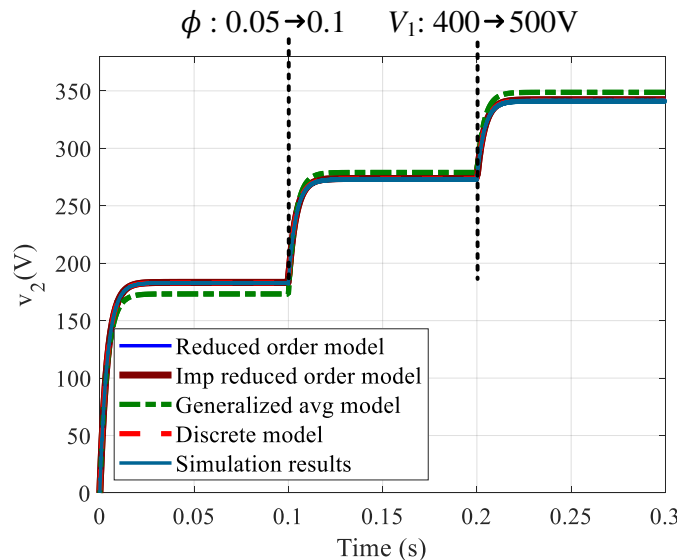

Fig. 10: The DAB circuit for model comparison.

Fig. 11: Comparison of large signal models.

TABLE II: Comparison of DAB modeling methods.

Modeling methods	Model complexity	Large signal accuracy	small signal accuracy
Reduced order [25]	Low	++++	++++
Imp reduced order [29]	Medium	++++	++++
Generalized average [31]	Medium	++	++
Discrete time [35], [37]	High	++++	++++

Note: **+ = Poor**; **++ = Average**; **+++ = Good**; **++++ = Excellent**

Fig. 11 shows comparison of the large signal models with simulation results, in which at $t = 0.1s$, the phase shift ratio
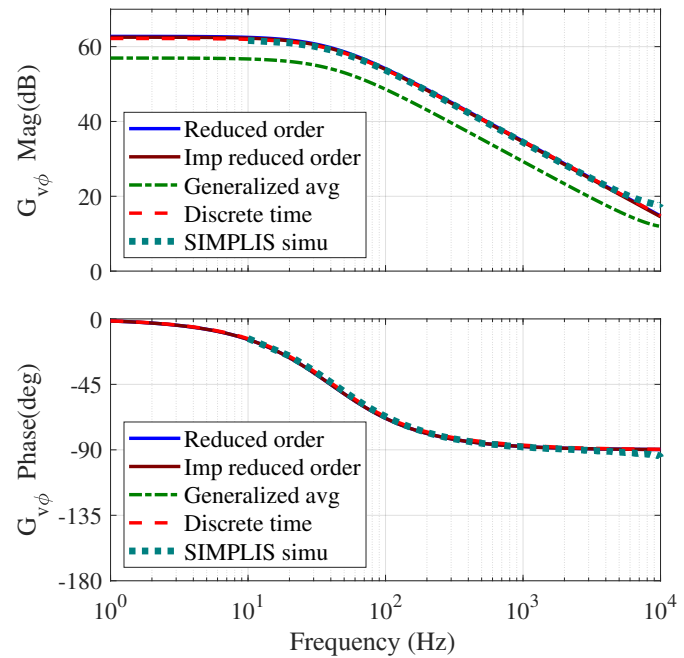

Fig. 12: Comparison of bode plot of small signal models $G_{v\phi}$ (from ϕ to v_2).

ϕ steps from 0.05 to 0.1, and at $t = 0.2s$, the input voltage V_1 steps from 400V to 500V. All the four models predict v_2 step response pretty well, however the generalized average model has some steady state errors because the third and higher order components of i_L are ignored.

Fig. 12 shows the bode plot of small signal models $G_{v\phi}(s)$ (open loop transfer function from ϕ to v_2) obtained using different modeling methods. For comparison, the simulated small signal response obtained through ac analysis in SIMetrix/SIMPLIS is also plotted. The operating conditions are $V_1 = 400V, \Phi = 0.1$, and other parameters are listed in Table I. Except for the generalized average model, all the other models correspond well to the simulated model both for the magnitude and phase. The generalized average model has a magnitude error because the third and higher order components of i_L are ignored.

Table II compares the performance of different modeling methods in terms of modeling accuracy and model complexity. The perfomance on the model accuracy is based on the results in Figs. 11 and 12, whereas the model complexity is based on the number of equations of each model. As shown in Table. II, the reduced order model [25] in Fig. 4 and Eq. (6) has the best overall performance and is recommended for closed-loop controller design in normal applications, due to its simplicity and good conformity to the simulation results. For high frequency DAB where the ZVS intervals have a significant impact on dynamics, the discrete-time model may be a better choice. Also note that the reduced order model, generalized average model and discrete-time model can be applied to a DAB modulated with DPS or TPS, and the related computation is more complex than that of the SPS.

The above analysis and simulation results suggest the DAB

is a first-order system, and the inductor L does not affect the DAB dynamic response. This interesting phenomenon may be explained as follows. The bipolar square voltages v_{ab} and v_{cd} of a DAB only have switching frequency f_s and its harmonics, and their dc components are 0, as shown in Figs. 2 and 3. The low frequency component (below $f_s/2$) of inductor current i_L, for instance the envelope in Fig. 46, cannot be transferred to dc side because of the orthogonality relations of the trigonometric functions:

$$\int_{t}^{t+T_s} \sin(n \cdot 2\pi f_s t + \phi_1) \cdot \sin(\omega_L t + \phi_2) dt = 0 \quad (2n\pi f_s \neq \omega_L)$$

(11)

where ω_L is the low frequency component of i_L. As result, the perturbation of i_L caused by disturbance such as change of input voltage or phase shift ratio cannot be propagated to output side, and the inductor L does not affect the DAB dynamic response. To further validate above analysis, Fig. 13 shows simulation results of the DAB output voltage v_2 with DAB circuit and the reduced order model (Fig. 4), where the DAB is controlled using the feedback-only control and the control parameters are listed in Table III. Under step change of the input voltage, load and output reference, the reduced order model predicts the DAB dynamic performance well.
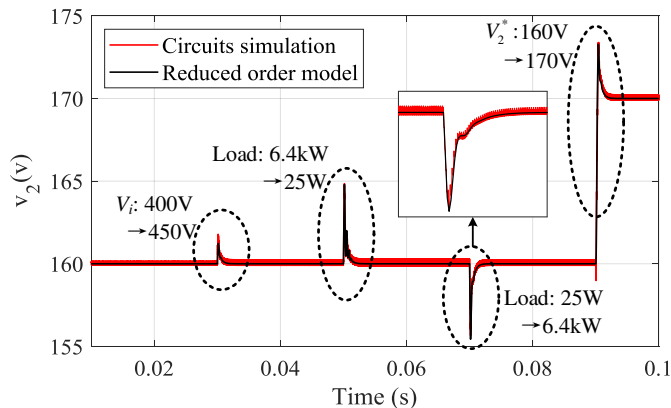

Fig. 13: Simulation results of the DAB output voltage v_2 with DAB circuit and the reduced order model.

III. CONTROL OF A DAB

This section mainly reviews the available output voltage control methods including conventional feedback control, linearization control, feedforward plus feedback control, disturbance observed based control, feedforward current control, predictive current control, sliding mode control and model predictive control.

To effectively evaluate and compare these output voltage control methods, the closed-loop control-to-output transfer function $G_{ro}(s)$ and the output impedance $Z_o(s)$ are selected as the metrics of the ability in voltage tracking and load current disturbance rejection. The transfer functions $G_{ro}(s)$ and $Z_o(s)$ of the feedback control, linearization control, feedforward plus feedback control are derived theoretically, and frequency
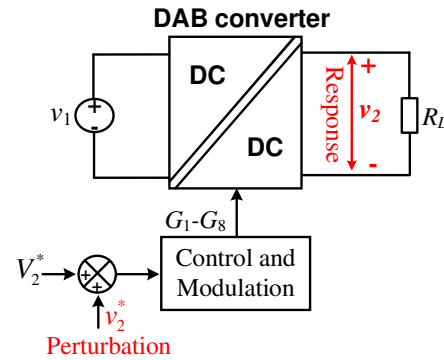

Fig. 14: The closed-loop transfer function evaluation circuit.
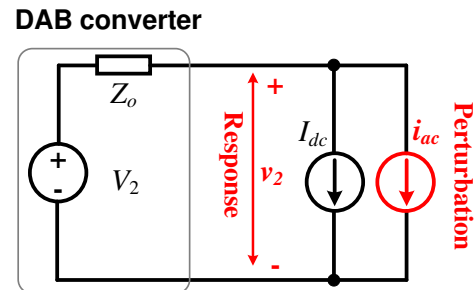

Fig. 15: The output impedance evaluation circuit.

response plots based on the derived transfer function are provided. $G_{ro}(s)$ and $Z_o(s)$ plots of the feedforward current control, predictive current control and mode predictive control are swept using simulation in Figs. 14 and 15.

In the reference to output ($G_{ro}(s)$) evaluation circuit Fig. 14, the reference signal consists of a DC component V_2^* and an AC component v_2^*. V_2^* sets the equilibrium point while v_2^* provides small signal perturbation (sine wave at certain frequency). The output voltage v_2 of the DAB converter is measured at each frequency of the reference perturbation v_2^*. $G_{ro}(s)$ can be obtained by calculating the magnitude and phase difference between v_2^* and v_2 at each frequency:

$$G_{ro}(f) = \frac{v_2(f)}{v_2^*(f)}$$

(12)

In the output impedance ($Z_o(s)$) evaluation circuit Fig. 15, the DAB converter is simplified as a voltage source V_2 and an output impedance Z_o. I_{dc} represents the steady-state load current which sets the equilibrium point, and i_{ac} stands for the injected small current which provides small signal perturbation. The output voltage v_2 of the DAB converter is measured at each frequency of the injected current i_{ac}. The output impedance can be obtained by calculating the magnitude and phase difference between v_2 and i_{ac} at each frequency:

$$Z_o(f) = \frac{v_2(f)}{i_{ac}(f)}$$

(13)

The evaluation circuit in Figs. 14 and 15 can be easily implemented using PLECS Multitone Analysis tool or SIMetrix/SIMPLIS. Based on the frequency response plots, remarks for each control method are drawn.

It is worth pointing out that the term "control method" here designates algorithms or circuits that takes only the sampling of the voltages and/or currents as inputs to generate the phase shift duties or active state duties of the DAB to track the output reference. By this definition, the so called "control" in the literature [39]–[42], are classified as the optimization of advanced modulations rather than control methods discussed here.

A. Feedback control on the output voltage

Feedback control with a proportional-integral (PI) compensator is the simplest method to regulate the output voltage. As shown in Fig. 16, the phase shift ratio ϕ between the primary and secondary bridges is modified dependent on the error in the output voltage [43], [44]. The PI compensator ($G_{c1}(s) = k_p + k_i/s$) is used to minimize the steady state error.
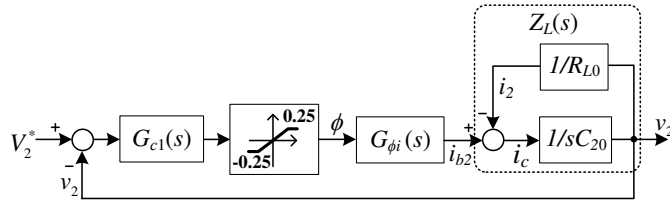

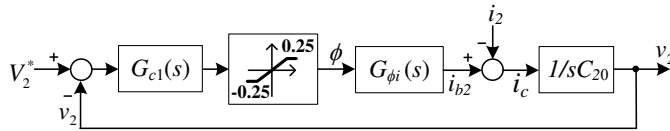
Fig. 16: Block diagram of feedback-only control.

Fig. 17: Block diagram to obtain the output impedance of the feedback-only control.

Considering the delay in the digital controller, the closed-loop control-to-output transfer function is derived based on Fig. 16 as:

$$G_{ro}(s) = \frac{v_2}{V_2^*} = \frac{G_{c1}G_{i\phi}Z_L e^{-1.5T_s s}}{1 + G_{c1}G_{\phi i}Z_L e^{-1.5T_s s}} \quad (14)$$

where $e^{-1.5T_s s}$ is delay caused by the sampling and digital control. The sampling and control delays are T_s and $0.5T_s$ respectively. The digital control delay $0.5T_s$ is caused by that the control variable ϕ updates once per switching cycle. This process can be modeled as a zero-order hold (ZOH), whose delay is $0.5T_s$.

$Z_L(s)$ is shown in Fig. 16 and can be expressed as:

$$Z_L(s) = \frac{R_L}{sC_2 R_L + 1} \quad (15)$$

To derive the output impedance $Z_o(s)$, the resistive load R_L is replaced with a current source i_2 in the DAB circuit as shown in Fig. 17. The output impedance can be developed as

$$Z_o(s) = \frac{v_2}{i_2} = -\frac{1/(sC_2)}{1 + G_{v1}G_{i\phi}e^{-1.5T_s s}/(sC_2)} \quad (16)$$
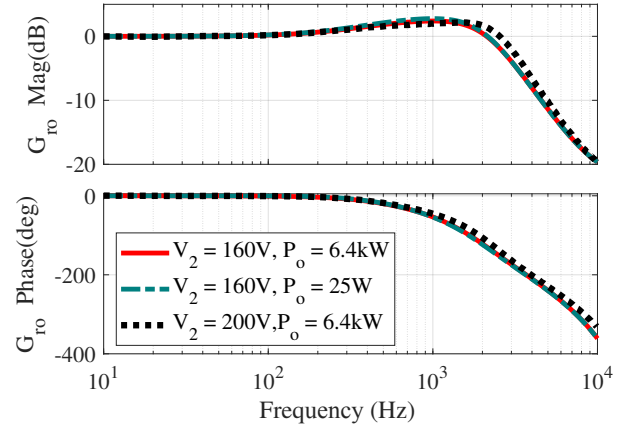
(a)
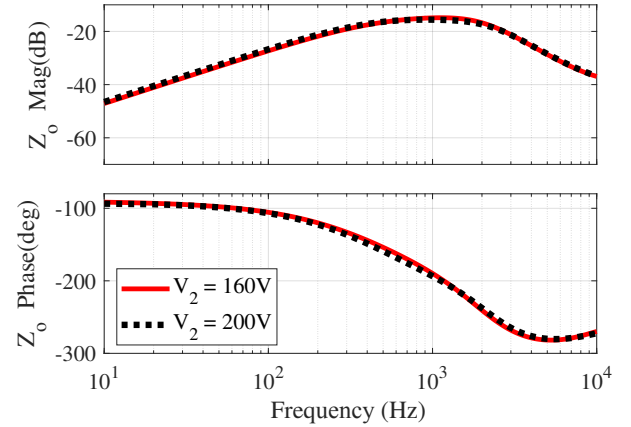
(b)

Fig. 18: Bode plot of the feedback only control: (a) $G_{ro}(s)$ under different load conditions, (b) $Z_o(s)$.

The PI parameters are designed to achieve 1.2kHz crossover frequency with $45°$ phase margin under full load ($R_L = 4\Omega, P_o = 6.4kW$) and we obtain $k_{p1} = 0.0193, k_{i1} = 37.6$. Fig. 18 shows the bode diagram of $G_{ro}(s)$ and $Z_o(s)$. Different load or output voltage conditions have minor influence on $G_{ro}(s)$ or $Z_o(s)$ as shown in Fig. 18.

B. Linearization control

A linearized control method is proposed in [45] to eliminate the nonlinear terms in DAB. The control can reduce the sensitivity of system stability to the load condition and reference voltage and help to enlarge the stable margin. Linearization control on the reduced order model is considered.

According to (2), the relationship between ϕ and i_{b2} is nonlinear:

$$\langle i_{b2} \rangle = \frac{NV_1\phi(1 - 2\phi)}{f_s L} \quad (17)$$

By solving (17), we obtain

$$\phi = \begin{cases} \dfrac{1}{4} - \sqrt{\dfrac{1}{16} - \dfrac{f_s L i_2}{2Nv_1}} & i_2 \geq 0 \\[3mm] -\dfrac{1}{4} + \sqrt{\dfrac{1}{16} + \dfrac{f_s L i_2}{2Nv_1}} & i_2 < 0 \end{cases} \quad (18)$$

Fig. 19: Block diagram of the linearization control with resistive load [45].

Fig. 20: Equivalent block diagram of the linearization control with resistive load.

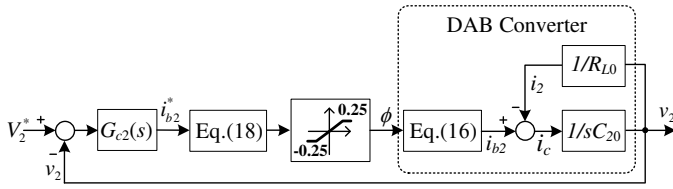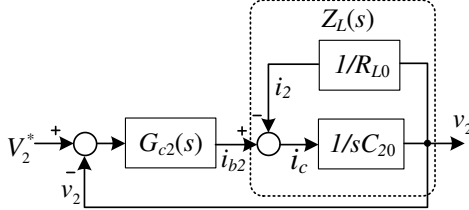The control block diagram of the linearization control is shown in Fig. 19, where Eq. (18) is inserted into the control loop. Since Eq. (18) is the solution of Eq. (17), the non-linearity of the control loop can be compensated. When the circuit parameters used in the control is exactly the same as that of the actual converter, then $i_{b2} = i_{b2}^*$ and Fig. 19 can be simplified as Fig. 20. The reference to output transfer function is:

$$G_{ro}(s) = \frac{G_{c2}Z_L e^{-1.5T_s s}}{1 + G_{c2}Z_L e^{-1.5T_s s}} \quad (19)$$

where $Z_L(s)$ is shown in (15). By replacing the resistor R_L with a current source (similar to that in Fig. 17), the output impedance can be calculated as:

$$Z_o(s) = -\frac{1}{sC_2 + G_{c2}e^{-1.5T_s s}} \quad (20)$$

The PI parameters are designed to achieve 1.2kHz crossover frequency with $45°$ phase margin under full load ($R_L = 4\Omega$) and we obtain $k_{p2} = 7.3155$, $k_{i2} = 1.425 \times 10^4$. Fig. 21 shows the bode plot of the linearization control based on (19) and (20). Theoretically, $G_{ro}(s)$ and $Z_o(s)$ of the linearization control will not be affected by output voltage or load conditions. However, when the circuit parameters in (18) are different from the actual ones, for instance $L = 0.8L_0$, the bandwidth of the DAB becomes narrower. Note L is the inductance used in the control, whereas L_0 is the inductance used in the actual DAB circuit (nominal value). Actually, according to Fig. 18, the closed-loop bandwidth and output impedance of the feedback-only control almost does not vary with different output voltage or load conditions, and the linearization may be not required.

C. Feedforward plus feedback control on output voltage

Combined feedforward plus feedback control can improve performance over simple feedback control as the disturbance can be measured and counterbalanced before it affects the process output.
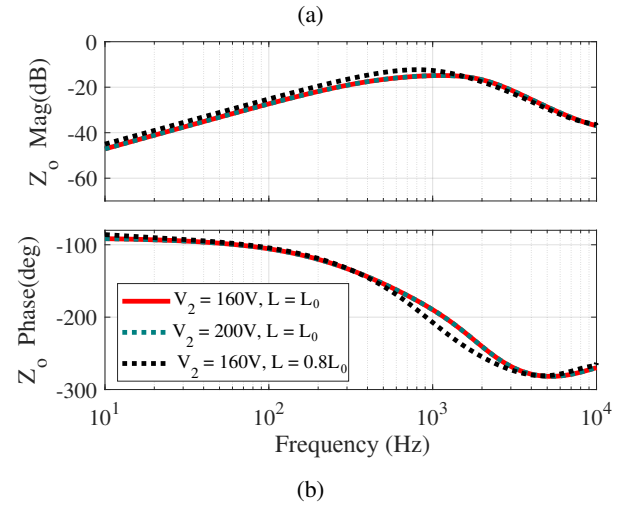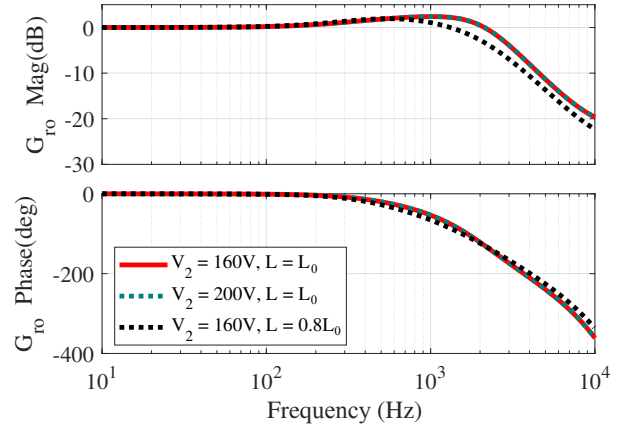
Fig. 21: Bode plot of the linearization control: (a) $G_{ro}(s)$, (b) $Z_o(s)$.

1) Output current feedforward (OCFF): The relationship of phase shift ratio ϕ and output power can be as a feedforward term to minimize error between the actual and desired behavior. Based on (1), the desired output power can be expressed as:

$$P_o^* = \frac{Nv_1 v_2 \Phi^*(1 - 2|\Phi^*|)}{f_s L} \quad (21)$$

Therefore the desired phase shift Φ^* can be calculated as:

$$\Phi^* = \begin{cases} \dfrac{1}{4} - \sqrt{\dfrac{1}{16} - \dfrac{f_s L i_2}{2Nv_1}} & i_2 \geq 0 \\[3mm] -\dfrac{1}{4} + \sqrt{\dfrac{1}{16} + \dfrac{f_s L i_2}{2Nv_1}} & i_2 < 0 \end{cases} \quad (22)$$
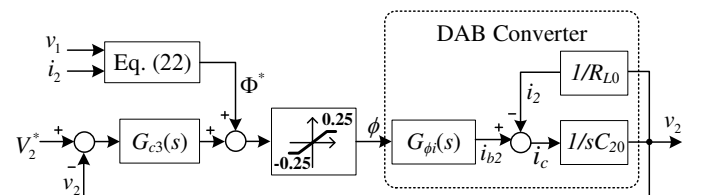
Fig. 22: Block diagram of the output current OCFF control.
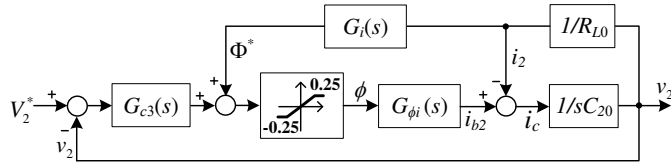
Fig. 23: Equivalent block diagram of the OCFF control.

Fig. 22 shows the control diagram, which is termed as output current feedforward (OCFF) control in this paper. Alternatively Φ^* can be generated using a lookup table [32].

To derive the transfer functions of $G_{ro}(s)$ and $Z_o(s)$, it is necessary to linearize (22) using small signal analysis. Assume the input voltage remains constant, local linearization of (22) yields:

$$G_i(s) = \frac{d\Phi^*}{di_2} = \begin{cases} \dfrac{f_sL}{4NV_1}\left(\dfrac{1}{16} - \dfrac{f_sLI_2}{2NV_1}\right)^{-\frac{1}{2}} & I_2 \geq 0 \\[3mm] \dfrac{f_sL}{4NV_1}\left(\dfrac{1}{16} + \dfrac{f_sLI_2}{2NV_1}\right)^{-\frac{1}{2}} & I_2 < 0 \end{cases} \tag{23}$$

where I_2 is the equilibrium value calculated as:

$$I_2 = \frac{NV_1\Phi(1-2\Phi)}{f_sL} \tag{24}$$

With the feedforward gain $G_i(s)$, the control block diagram of Fig. 22 can be transformed to Fig. 23. The closed-loop control-to-output transfer function $G_{ro}(s)$ is derived based on Fig. 23 as

$$G_{ro}(s) = \frac{G_{c3}G_{i\phi}Z_Le^{-1.5T_ss}}{1+(G_{c3}G_{i\phi}-G_iG_{i\phi}/R_L)Z_Le^{-1.5T_ss}} \tag{25}$$

where $Z_L(s)$ is shown in (15). To derive the output impedance, the resistive load R_L in Fig. 23 is replaced with a current source (similar to the transformation from Fig. 16 to Fig. 17). The output impedance of the OCFF control can be calculated as

$$Z_o(s) = \frac{(G_iG_{i\phi}e^{-1.5T_ss}-1)/(sC_2)}{1+G_{c3}G_{i\phi}e^{-1.5T_ss}/(sC_2)} \tag{26}$$

Based on (3) and (23), when the circuit parameters used in the control are exact the same as the actual ones ($L = L_0$), we can calculate:

$$G_iG_{\phi i} = 1 \tag{27}$$

Ignore the control delay $e^{-1.5T_ss}$ and substitute (27) into (25) and (26), we obtain

$$G_{ro}(s) = \frac{G_{c3}G_{i\phi}}{sC_2+G_{c3}G_{i\phi}} \tag{28}$$

$$Z_o(s) = 0 \tag{29}$$

In (28), the feedforward term $G_i(s)$ eliminates the influence of R_L on $G_{ro}(s)$. In (29), the output impedance $Z_o(s)$ becomes zero with the feedforward gain G_i, indicating perfect load disturbance rejection capability. However, the results in

(a)

(b)
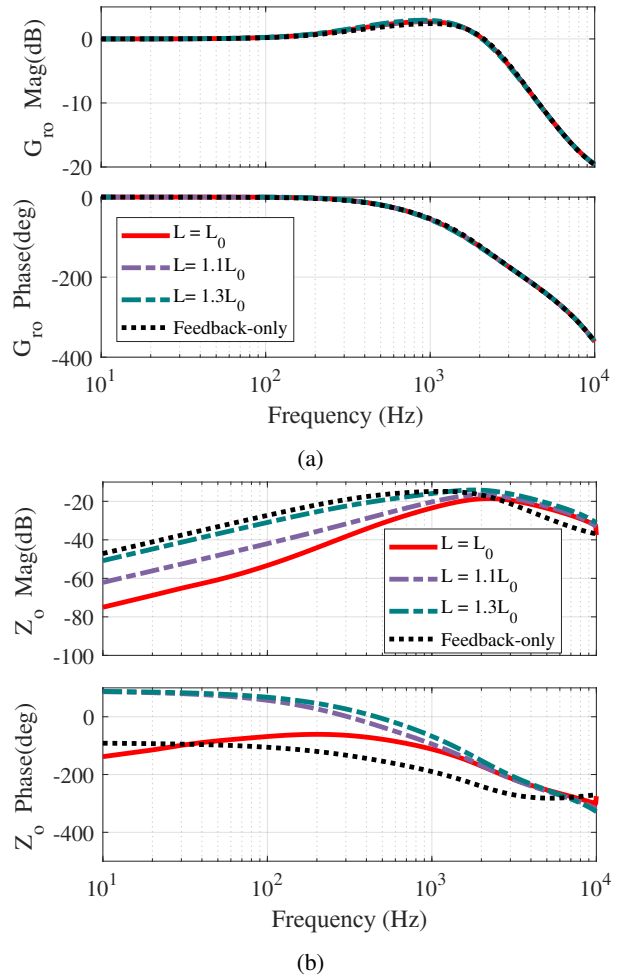
Fig. 24: Bode plot of the OCFF control: (a) $G_{ro}(s)$, (b) $Z_o(s)$.

(28) and (29) are valid only when the circuit parameters used in the control are exact the same as the actual ones.

Assume L used in the control is $1/\alpha$ times of actual inductance L_0:

$$L = L_0/\alpha \tag{30}$$

Based on (4)(23)(30), when $I_2 > 0$ the transfer function $G_i(s)$ becomes

$$G_i(s) = \frac{d\Phi^*}{di_2} = \frac{f_sL}{4\alpha NV_1}\left(\frac{1}{16} + \frac{\Phi^2 - \Phi/2}{\alpha}\right)^{-\frac{1}{2}} \tag{31}$$

where Φ is the quiescent value of ϕ shown in (4).

Multiplying (3) to (31), we calculate

$$G_{\phi i}G_i = \frac{(1-4\Phi)}{\alpha}\left(1 + \frac{16\Phi^2 - 8\Phi}{\alpha}\right)^{-0.5}$$
$$\neq 1 \quad \text{(when } \alpha \neq 1\text{)} \tag{32}$$

The PI parameters are designed to achieve 1.2kHz crossover frequency with $45°$ phase margin under full load ($R_L = 4\Omega$) and we obtain $k_{p3} = 0.0193, k_{i3} = 37.6$. Fig. 24 shows the bode plots of $G_{ro}(s)$ and $Z_o(s)$ of the OCFF control based on (25) and (26). As shown in Fig. 24 (b), when $L = L_0$, the magnitude of Z_o of the OCFF control is much smaller

than that of the feedback only control. However, when $L = 1.1L_0$, the magnitude of $Z_o(s)$ increases; when $L = 1.3L_0$, the magnitude of $Z_o(s)$ becomes the same as that of the feedback only control.

The results in Fig. 24 tell that the OCFF control needs the accurate acquisition of the circuit parameters in order to achieve good load disturbance rejection. The practical performance of the OCFF control may not be as good as designed. Similar methods are also found in [46], [47].

2) Virtual Direct Power Control: Another feedforward control termed as Virtual Direct Power Control (VDPC) has been proposed in [48]. The advantage of the VDPC is that it eliminates the necessity of using the information of the inductance L by using the unified power to calculate Φ^*.
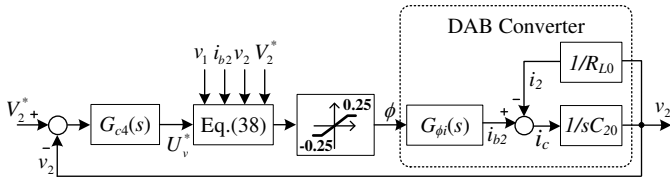
Fig. 25: Block diagram of the VDPC control [48].

In this method, a virtual power reference p^* is defined

$$p^* = |U_v^*|i_2^*, \tag{33}$$

where $|U_v^*|$ is named as the virtual desired output voltage, which is output value of the PI compensator in Fig. 25. Assuming a resistive load, the desired output current i_2^* can be described as:

$$\frac{i_2^*}{V_2^*} = \frac{i_2}{v_2} \tag{34}$$

Substituting i_2^* from (34) into (33) yields

$$p^* = \frac{|U_v^*| V_2^*}{v_2} i_2 \tag{35}$$

On the other hand, the unified power is expressed as:

$$P_{pu} = P_o/P_{base} = V_1 v_2 \phi(1 - 2|\phi|) \tag{36}$$

where the unity base is

$$P_{base} = 1/(f_s L) \tag{37}$$

Let $P_{pu} = p^*$, we can calculate

$$\phi = \begin{cases} \frac{1}{4} - \sqrt{\frac{1}{16} - \frac{V_2^* U_v^* i_2}{4v_2^2 v_1}} & i_2 \geq 0 \\ -\frac{1}{4} + \sqrt{\frac{1}{16} + \frac{V_2^* |U_v^*| i_2}{4v_2^2 v_1}} & i_2 < 0 \end{cases} \tag{38}$$

In essence, the VDPC utilizes the virtual voltage U_v^* to avoid involving any circuit parameters such as the switching frequency f_s, inductance L or transformer turn ratio N. The circuit parameter uncertainty has no influence on the control loop theoretically.

Similar to the OCFF control method, the closed-loop reference to output transfer function $G_{ro}(s)$ and output impedance $Z_o(s)$ can be calculated. The PI parameters are designed as
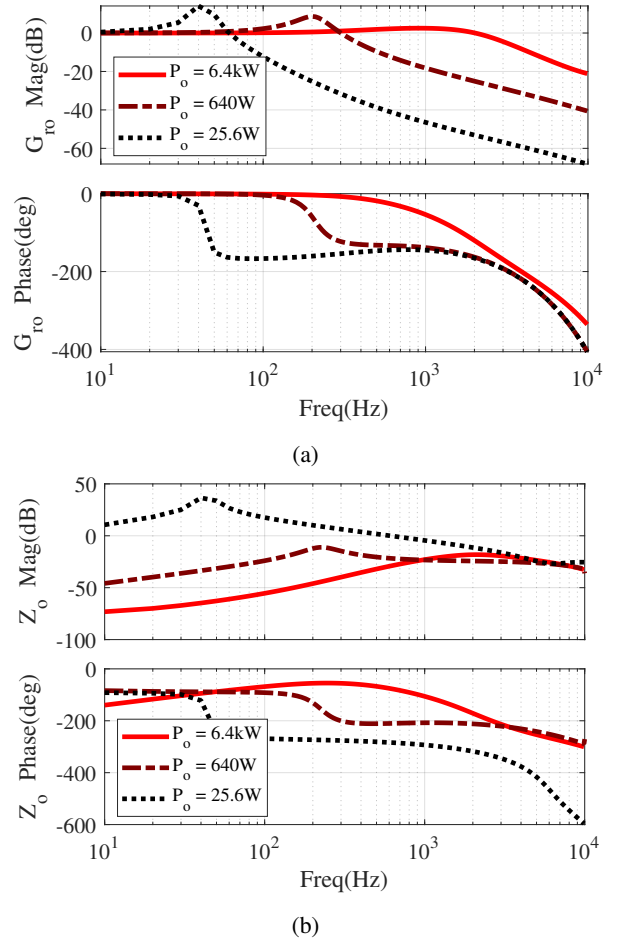
Fig. 26: Bode plot of the VDPC control: (a) $G_{ro}(s)$, (b) $Z_o(s)$.
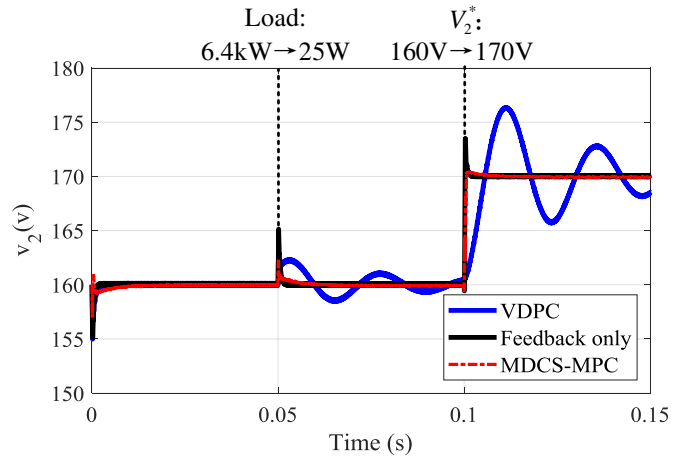
Fig. 27: Time domain simulation results of the VDPC, feedback-only and MDCS-MPC [48].

$k_{p4} = 38.524, k_{i4} = 1.068 \times 10^5$. Fig. 26 shows the bode plot of $G_{ro}(s)$ and $Z_o(s)$.

However, the VDPC can have poor dynamic performance under light load conditions. Under light load condition, i.e., $i_2 \approx 0$, the output of Eq. (38) is close to 0 and the VDPC loop gain will be small since (38) is inside the control loop. Fig. 26 shows the bode plot of $G_{ro}(s)$ and $Z_o(s)$ under

different load conditions. Under the condition $P_o = 25W$, the control bandwidth drops significantly (Fig. 26(a)). As a result, the output impedance increase significantly (Fig. 26(b)). The narrow bandwidth and high output impedance indicate poor performance on voltage tracking and load current disturbance rejection. The above observation is further validated using the time domain simulation results in Fig. 27. When the load steps to light at 0.05s, the dynamic performance becomes poor.

D. Disturbance-Observer-Based Control

In the above feedforward control methods, OCFF control can significantly reduce the output impedance and improve the load disturbance rejection capability. However, its performance deteriorates quickly in the presence of parameter uncertainty. The VDPC tries to solve the parameter sensitivity problem by using the PI output to estimate the phase shift, but its loop gain is too low under light load conditions. Besides, an additional current sensor is required in these feedforward control methods.

Disturbances and uncertainties exist in all power converter control systems [49]. These disturbances and uncertainties include input voltage and load variation, model uncertainty, and circuit parameter variations due to temperature or aging effects [50]. Disturbance-observer-based control (DOBC) employs an observer to estimate the total disturbances and uncertainties, and corresponding compensation is then generated by making use of the estimate [49]. Therefore the DOBC can achieve superior control performance. The input to the disturbance observer is the output voltage v_2 and control signal (phase shift ratio ϕ), no additional current sensor is required [50], [51].

DOBC for the DAB converter has been introduced in [50]–[52]. The derivation procedures of the disturbance observer from [50] are briefly repeated here to illustrate its basic principles.

According to Fig. 4, we can obtain the following small signal equation

$$\frac{d\hat{v}_2}{dt} = \frac{NV_1(1-4\Phi)}{f_s L C_2}\hat{\phi} - \frac{\hat{v}_2}{R_L C_2} \tag{39}$$

Rearrange (39), we can get

$$\frac{d\hat{v}_2}{dt} = f_t\left(\hat{v}_2, \hat{\phi}\right) + b_0\hat{\phi} \tag{40}$$

where $f_t\left(\hat{v}_2, \hat{\phi}\right) = a\hat{v}_2 + (b - b_0)\hat{\phi}$ is the total disturbance which includes external disturbances, circuit parameter variations, and model uncertainties, with

$$a = -\frac{1}{R_L C_2}, b = \frac{NV_1(1-4\Phi)}{f_s L C_2}, b_0 = \frac{NV_{10}(1-4\Phi_0)}{f_s L_0 C_{20}}$$

where V_{10}, L_0 and C_{20} are the nominal values of the input voltage, inductance, and output capacitance respectively.

The disturbance observer for the DAB can be designed as follows

$$\frac{d\tilde{v}_2}{dt} = \tilde{f}_t + \beta_1\left(\hat{v}_2 - \tilde{v}_2\right) + b_0\hat{\phi} \tag{41}$$

$$\frac{d\tilde{f}_t}{dt} = \beta_2\left(\hat{v}_2 - \tilde{v}_2\right) \tag{42}$$

where $\tilde{v}_2$ and $\tilde{f}_t$ are the estimated values of $\hat{v}_2$ and f_t respectively.

Define the estimation error $e_1 = \hat{v}_2 - \tilde{v}_2$ and $e_2 = f_t - \tilde{f}_t$, then the following equations can be derived considering (40), (41) and (42):

$$\begin{cases} \dot{e}_1 = e_2 - \beta_1 e_1 \\ \dot{e}_2 = \dot{f}_t - \beta_2 e_1 \end{cases} \tag{43}$$

By choosing β_1 and β_2 positive, then e_1 and e_2 converge to zero exponentially, i.e., the estimated states will converge to the actual states [50].

Choose $\beta_1 = 2\zeta\omega_n$ and $\beta_2 = \omega_n^2$. Rearrange the disturbance observer (41) and (42) as follows:

$$\dot{\mathbf{X}} = \mathbf{A}\mathbf{X} + \mathbf{B}\mathbf{U} \tag{44}$$

where

$$\mathbf{X} = \begin{bmatrix} \tilde{v}_2 \\ \tilde{f}_t \end{bmatrix} \quad \mathbf{A} = \begin{bmatrix} -2\zeta\omega_n & 1 \\ -\omega_n^2 & 0 \end{bmatrix}$$

$$\mathbf{B} = \begin{bmatrix} b_o & 2\zeta\omega_n \\ 0 & \omega_n^2 \end{bmatrix} \quad \mathbf{U} = \begin{bmatrix} \hat{\phi} \\ \hat{v}_2 \end{bmatrix}$$

From (44), the transfer functions from ϕ and v_2 to $\tilde{f}_t$ can be derived as follows:

$$G_{f\mu}(s) = \frac{\tilde{f}_t}{\hat{\phi}} = \frac{-\omega_n^2 b_o}{s^2 + 2\zeta\omega_n s + \omega_n^2} \tag{45}$$

$$G_{fv}(s) = \frac{\tilde{f}_t}{\hat{v}_2} = \frac{\omega_n^2 s}{s^2 + 2\zeta\omega_n s + \omega_n^2} \tag{46}$$
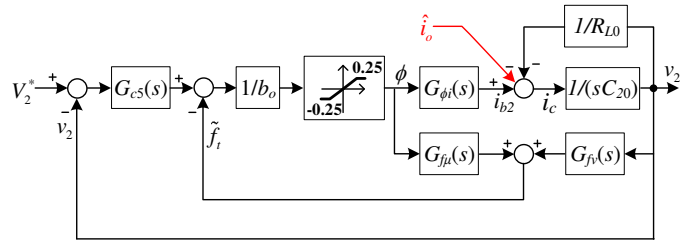
Fig. 28: Block diagram of the disturbance observer based control [50].

Fig. 28 shows the block diagram of the DOBC. The estimated disturbance $\tilde{f}_t$ is subtracted to compensate the actual disturbance in the control system. Loop gain of the control system can be calculated as:

$$G_o(s) = \frac{G_{c5}(s)G_{\phi i}Z_L e^{-1.5T_s s} b_o^{-1}}{1 + (G_{fv}G_{\phi i}Z_L + G_{f\mu})e^{-1.5T_s s} b_o^{-1}} \tag{47}$$

The PI parameters of $G_{c5}(s)$ are designed to achieve 1.2kHz crossover frequency with $45°$ phase margin under full load ($R_L = 4\Omega$). When $L = L_0, C_2 = C_{20}$, we obtain $k_{p5} = 7.53 \times 10^3, k_{i5} = 1.37 \times 10^7$. These control parameters are large because of the gain $1/b_o$ in the control loop in Fig. 28, where $b_o = 3 \times 10^5$ in this design. After multiplying this gain, the PI parameters of DOBC are of the same order of magnitude of that of other control methods.

(a)

(b)
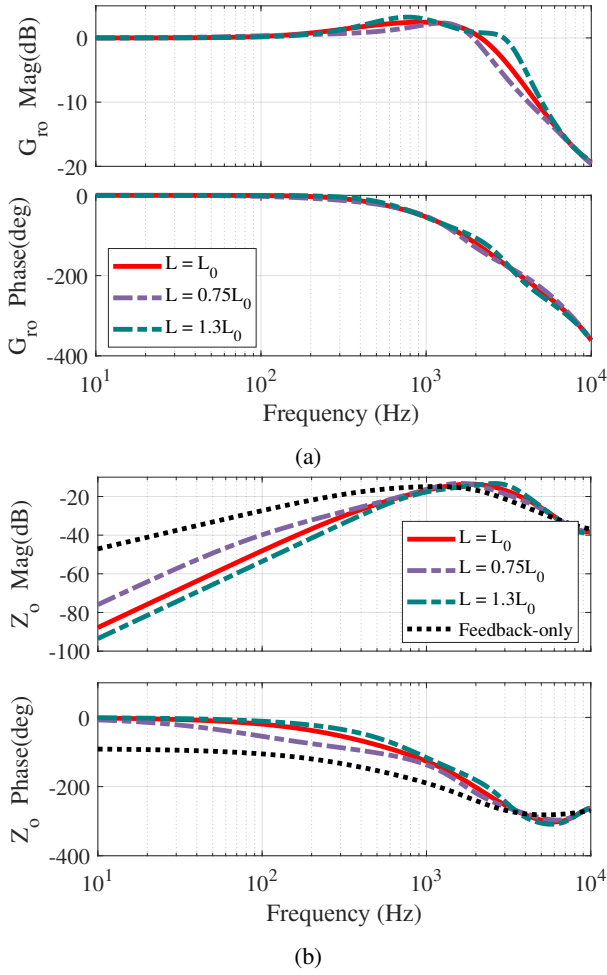
Fig. 29: Bode plot of the DOBC control: (a) $G_{ro}(s)$, (b) $Z_o(s)$.

The output impedance can be calculated as follows:

$$Z_o(s) = \frac{-1}{sC_2 + (G_{c5} + G_{fv})\dfrac{e^{-1.5T_s s}b_o^{-1}}{1 + G_{f\mu}e^{-1.5T_s s}b_o^{-1}}G_{\phi i}} \quad (48)$$

Fig. 29 shows the bode plots of $G_{ro}(s)$ and $Z_o(s)$ of the DOBC based on (47) and (48). According to Fig. 29(b), the output impedance of the DOBC is much smaller than that of the feedback-only control, indicating better load disturbance rejection capability. Besides, the performance of the DOBC is not sensitive to the parameter variation. These superior performance is due to the load disturbance and parameter uncertainties are estimated and compensated by the disturbance observer in the DOBC.

E. Current mode control

The common feature of this category is that the transformer current is involved in the control. The information of the transformer current can improve the dynamic performance and provide a way to limit the peak transformer current.

1) Feed-Forward Current Control: A Feed-Forward Current Control (FFCC) is introduced by *Z. Shan et al* [53] with the transformer instant current being regulated similar to the
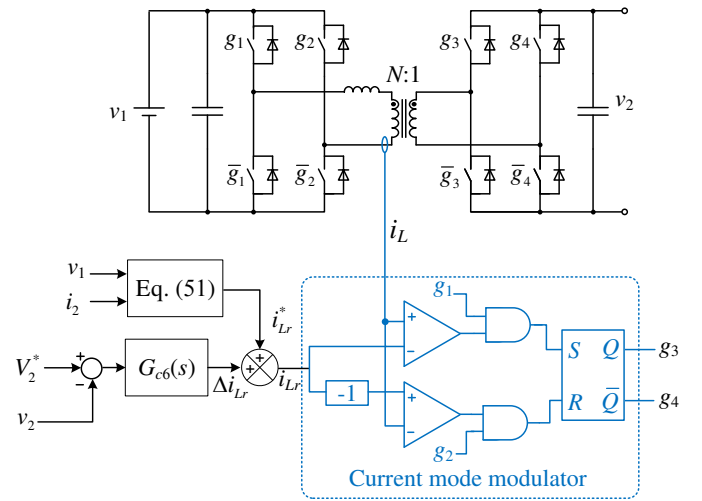
Fig. 30: Block diagram of the current mode control with feedforward of load current [53].
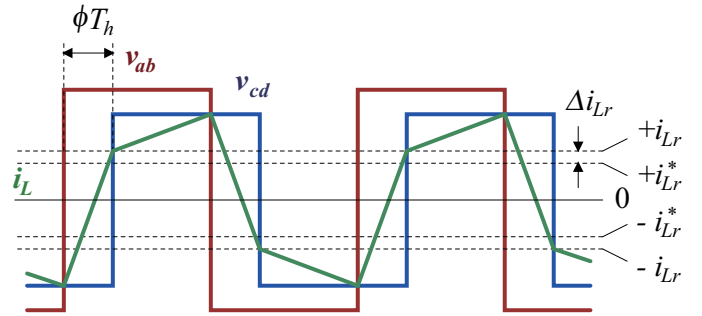
Fig. 31: Key waveforms of the current mode control in [53].

peak current control in [54]. The control block diagram when the power transfer from primary to secondary side is shown in Fig. 30 and typical waveforms are shown in Fig. 31. With a SR flip-flop, the secondary bridge is commutated at the time instant when the transformer current is equal to a reference i_{Lr} (Fig. 30 and 31).

The inductor current i_L changes from i_{Lr} to $-i_{Lr}$ from time ϕT_s to $(1/2 + \phi)T_s$, therefore

$$i_{Lr} = \frac{Nv_2 - v_1(1 - 4\phi)}{4f_s L} \quad (49)$$

According to (2) and (49), we calculate

$$i_{Lr} = \frac{i_2}{N}\frac{2}{1 + \sqrt{1 - \dfrac{8i_2 L f_s}{v_1 N}}} - \frac{v_1 - Nv_2}{4L f_s} \quad (50)$$

Since the term $(v_1 - Nv_2)/(4Lf_s)$ has slower time variation and can be compensated using the feedback term Δi_{Lr} in Fig. 30, (50) can be simplified as:

$$i_{Lr}^* = \frac{i_2}{N}\frac{2}{1 + \sqrt{1 - \dfrac{8i_2 L f_s}{V_1 N}}} \quad (51)$$

With the FFCC, fast changes on i_2 or V_2^* will lead to an immediate change at i_{Lr}^* to enable a fast response.

During the transient period, the inaccuracy on the feedforward algorithm is compensated by the PI feedback controller. Since the transformer current is directly manipulated, the transient dc-offset current on the DAB transformer can be inherently eliminated.

The open-loop bode plot of FFCC control (Fig. 30) can be swept using PLECS multitone analysis tool. Based on the swept open-loop bode plot, the PI compensator for the FFCC control are designed to achieve 1.2kHz crossover frequency with $45°$ phase margin, and the resultant PI parameters are: $k_{p6} = 4.35, k_{i6} = 3.17 \times 10^4$.

The bode plots of $G_{ro}(s)$ and $Z_o(s)$ of the FFCC are swept using the evaluation circuits Figs. 14 and 15 in the software PLECS. The swept $G_{ro}(s)$ and $Z_o(s)$ are shown in Fig. 32, where L_0 is the actual inductance in DAB and L is the inductance value used in the FFCC control. With the feedforward term and current mode control, the output impedance of the FFCC is the smallest compared to Feedback only control and OCFF control. Besides, in the presence of the parameter variation, the performance of the FFCC control degrades less significantly compared to the OCFF control (Fig. 24). Even when $L = 1.3L_0$, the output impedance of FFCC control is still much smaller than the feedback-only control.

Just like other peak current control method, the FFCC is susceptible to noise. A noise spike is generated each time the power devices switch. The spike can be large when the DAB loses zero voltage switching (ZVS). A fraction of a volt coupled into the control circuit can cause the switch turn off immediately, resulting subharmonic operating mode with much greater ripple [55]. Possible solutions to suppress the sampling noise and to avoid subharmonic oscillations include: 1) Operation of DAB in ZVS-on region, 2) Utilization of the isolated current sensor, 3) Addition of the filter on the sampled current. In addition, the logic circuit of the current mode modulator can be complex when the DAB operating bidirectionally.

2) Predictive current control: Another digital predictive current control is proposed by *S. Dutta et al.* [56], [57]. As shown in Fig. 33, the phase shift ϕ can be calculated as:

$$\phi = \frac{i_{r1} - i_{r0}}{T_s} \frac{L}{v_1 + Nv_2} \tag{52}$$

With (52), the block diagram of the predictive current control is illustrated in Fig. 34. i_{r1} is generated by the compensator, whereas i_{r0}, v_1 and v_2 are sampled each switching cycle.

The open loop bode plot of the predictive current control can be swept using the PLECS multitone analysis tool. Based on the swept results, the PI compenesator for the predictive control is designed to achieve 1.2kHz crossover frequency with $45°$ phase margin, the resultant PI parameters are $k_{p7} = 24.8, k_{i7} = 1.45 \times 10^5$.

The bode plots of $G_{ro}(s)$ and $Z_o(s)$ of the predictive current control are swept using the evaluation circuits obtained using the software PLECS. The results are shown in Fig. 35. Parameter tolerance is considered $L = 1.1L_0$. The output impedance of the predictive current control is smaller than
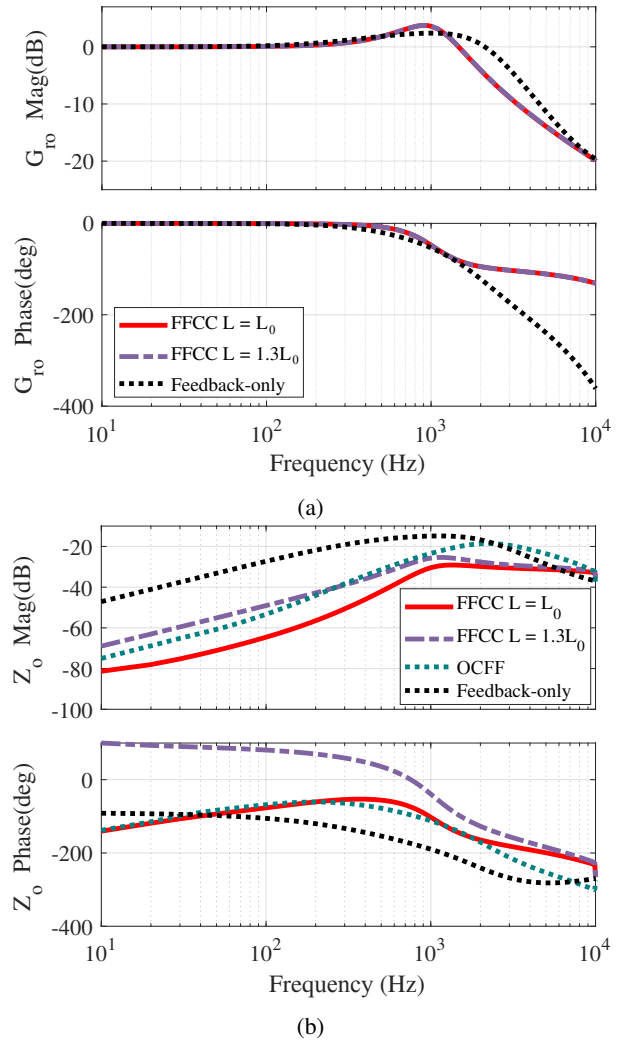
Fig. 32: Bode plot of the FFCC control: (a) $G_{ro}(s)$, (b) $Z_o(s)$.
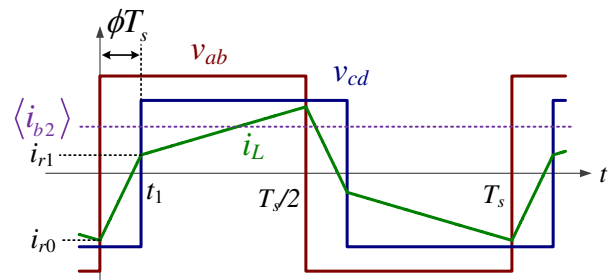

Fig. 33: DAB waveforms

.

that of the feedback only control, but higher than that of the FFCC.

The predictive current control requires ac current sampling and intensive computation in one switching period. For DAB converters with wide bandgap devices where switching frequency could range from 100kHz – 1MHz [15], [58], it is challenging to implement this predictive current control.
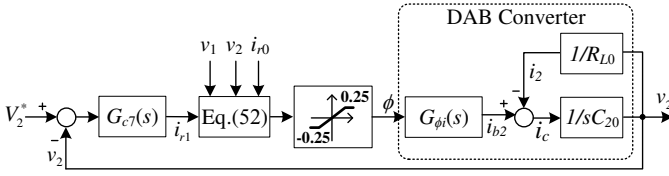
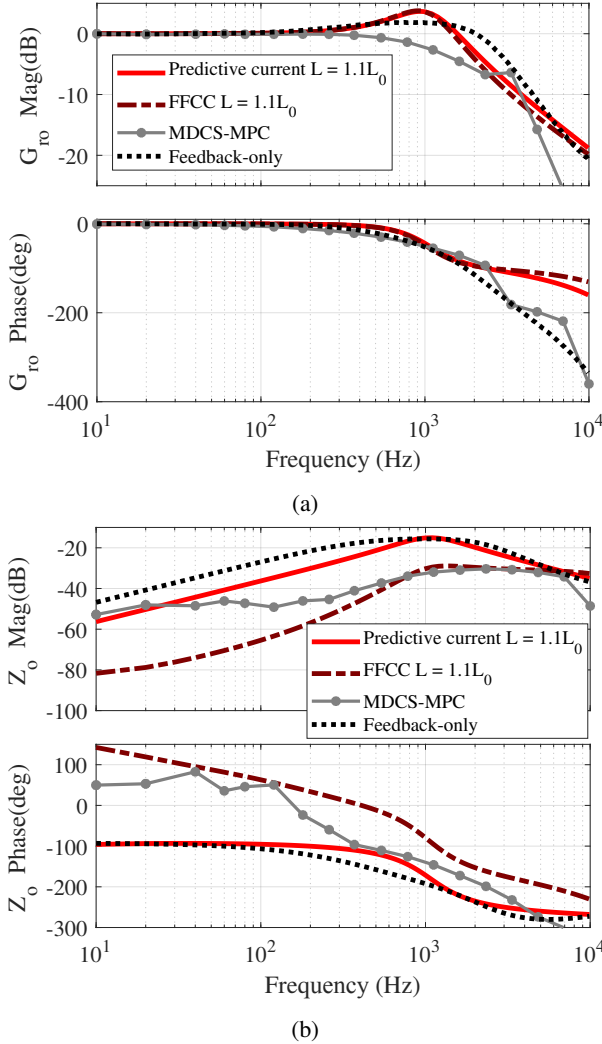Fig. 34: Block diagram of the predictive current control [56], [57]

Fig. 35: Frequency response plot comparison of the predictive current control, FFCC, MDCS-MPC and feedback only control: (a) $G_{ro}(s)$, (b) $Z_o(s)$.

F. Sliding mode control

Small-signal models and analysis have been widely used in the power electronics for stability assessment. However, they fail to predict the stability of some converters in presence of large transient. Worse still, the small-signal model fails to reveal any stability information of the converter over the entire operating region [59]. In the works [60], [61], it is shown that even though stable operation is concluded from the small-signal analysis, the system can be unstable. The main

advantage of a system with sliding mode control (SMC) is that it has guaranteed stability and robustness against parameter uncertainties [62].

The SMC has been applied to the DAB converter in [63] based on generalized average model and in [64] based on the reduced order model. According to Section II, the reduced order model presents better accuracy compared to the generalized average model, therefore the SMC is introduced with the reduced order model.

In general, assume the dynamic equation of a system is:

$$\frac{dx}{t} = f + gu \tag{53}$$

where x is the state variable, f and g are function of x, u is the discontinuous control action expressed as:

$$u = \begin{cases} U^+ & \text{if } S(x,t) > 0 \\ U^- & \text{if } S(x,t) < 0 \end{cases} \tag{54}$$

where U^+ and U^- are either scalar values or scalar functions of x. $S(x,t)$, usually called the sliding mode surface, is the instantaneous feedback tracking trajectory of the system and is predetermined function of the state variable [59]. Typically, $S(x,t)$ is chosen as a linear combination of weighted values of the state variables:

$$S(x,t) = \sum_{i=1}^{m} \alpha_i x_i \tag{55}$$

The ideal sliding mode action described in (54) is similar to the on and off bang-bang control which results in the high-frequency oscillation within the vicinity of the sliding surface while moving towards origin. Alternatively, equivalent control has been used to replace (54). The equivalent control action is obtained by solving (56). This is called the invariance condition [59].

$$\frac{dS(x,t)}{dt} = 0 \tag{56}$$

The steady state error that occurs with the SMC (54) can be minimized by comprising an integral term of the state variable into the sliding surface [65]. This approach is called integral SMC. However, the integral SMC becomes less effective when equivalent control action is implemented [66]. Therefore, *S. C. Tan et al.* proposed an additional double integral term of the state variables for construction of the sliding surface when the equivalent SMC is utilized [67].

In the DAB converter, state variables are chosen to be [68]:

$$x = [x_1, x_2, x_3]^T = [v_{err}, \int_0^t v_{err} dt, \int_0^t x_2 dt]^T \tag{57}$$

where $v_{err} = V_2^* - v_2$.

According to Fig. 4 and (2), the state equation of the DAB can be written as:

$$\frac{dv_2}{dt} = -\frac{v_2}{C_2 R_L} + \frac{v_1}{C_2 f_s L} \phi (1 - 2|\phi|) \tag{58}$$

According to the double integration approach [67], the sliding surface is constructed as:

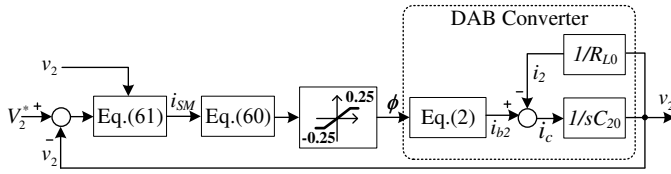$$S(x,t) = \sum_{i=1}^{3} \alpha_i x_i \tag{59}$$

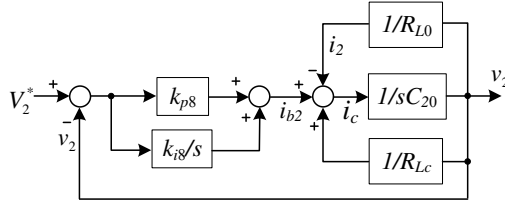Fig. 36: Block diagram of the sliding mode control [68].

Fig. 37: Equivalent block diagram of the SMC with resistive load.

According to the invariance condition (56), the equivalent control law can be derived as:

$$\phi = \begin{cases} \dfrac{1}{4} - \sqrt{\dfrac{1}{16} - \dfrac{f_s L i_{SM}}{2v_1}} & i_{SM} \geq 0 \\[3mm] -\dfrac{1}{4} + \sqrt{\dfrac{1}{16} + \dfrac{f_s L i_{SM}}{2v_1}} & i_{SM} < 0 \end{cases} \quad (60)$$

i_{SM} used in (60) can be expressed as [68]:

$$i_{SM} = \frac{v_2}{R_{Lc}} + C_2 \frac{\alpha_2}{\alpha_1} v_{err} + C_2 \frac{\alpha_3}{\alpha_1} \int_0^t v_{err} dt \quad (61)$$

where R_{Lc} is the load resistance value used in the control.

Different from (18), i_{SM} in (60) is a virtual current generated by (61). Based on (60) and (61), the SMC control diagram is shown in Fig. 36. Essentially, Eq. (61) is PI compensator plus a feedforward term. Besides, Eq. (60) is the solution of Eq. (18), similar to the linearization control. Therefore, the SMC block diagram Fig. 36 can be equivalent to Fig. 37, where $k_{p8} = C_2\alpha_2/\alpha_1$, $k_{i8} = C_2\alpha_3/\alpha_1$,

Based on Fig. 37, the PI parameters of the SMC is designed to achieve 1.2kHz crossover frequency with $45°$ phase margin: $k_{p8} = 7.3155, k_{i8} = 1.425 \times 10^4$, which is the same as that of the linearization control. Similar to the linearization control, the transfer functions of $G_{ro}(s)$ and $Z_o(s)$ can be derived according to Fig. 37. Fig. 38 shows bode plots of $G_{ro}(s)$ and $Z_o(s)$ of the SMC control. The feedforward term R_{Lc} actually does not affect $G_{ro}(s)$ or $Z_o(s)$, and the bode plots of the SMC are exact the same as that of the linearization control. When the inductance value L used in the control is different from the actual one (L_0) in the circuit, the control bandwidth becomes narrower and the output impedance increases.

G. Predictive control on output voltage

The utilization of predictive controls on the DAB generally provides salient dynamic performance. They draw on the information of the circuit to calculate the optimal value for the future control variables.

A moving discretized control set model predictive control (MDCS-MPC) is proposed by *L. Chen et al.* [69], [70]. The
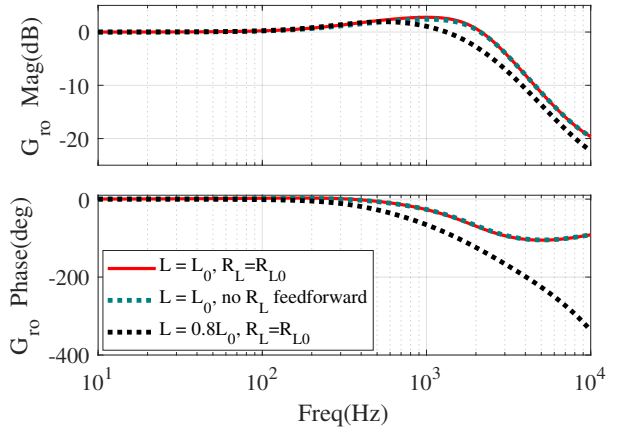
(a)
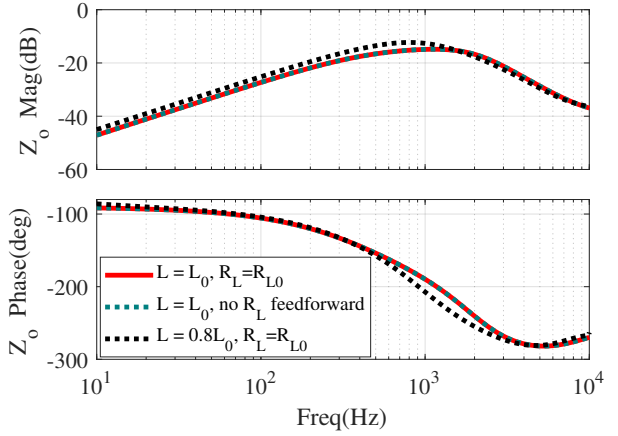
(b)

Fig. 38: Frequency response plot of the SMC: (a) $G_{ro}(s)$, (b) $Z_o(s)$.

phase shift ratio ϕ is divided into the discretized elements to fit digital control.

According to (1) and Fig. 5, the DAB output voltage is regulated by the phase shift ϕ, which is continuous in nature. To adapt digital control, ϕ needs to be discretized. Consider a commercial micro-controller with a peripheral clock f_c (Fig. 39), the finest phase shift value Δ_f is:

$$\Delta_f = \frac{f_c}{f_s}, \quad (62)$$

where f_s is the DAB switching frequency.

The range of the DAB phase shift ratio is:

$$\phi \in [-0.25, 0.25] \quad (63)$$

The above ϕ can be further discretized into $\mu_m (= 1/\Delta_f + 1)$ elements as described in array:

$$\phi \in \{-0.25, \cdots, 0, \Delta_f, 2\Delta_f, \cdots, 0.25\} \quad (64)$$

Taking into account the computational delay, MDCS-MPC has a prediction horizon of two sampling periods. To illustrate the principle of MDCS-MPC, consider a cost function in (65) that only regulating the output voltage v_2 to the reference V_2^*

$$ct = (V_2^* - v_2[k+2])^2 \quad (65)$$

This cost function is executed during the time instant $[k, k+1]$ and $v_2[k+2]$ is the predicted output voltage at time instance $k+2$ and can be calculated based on Fig. 4 [69]:

$$v_2[k+2] = \frac{i_{b2}[k+1] + i_{b2}[k] - 2i_2[k]}{C_2 f_s} + v_2[k] \qquad (66)$$

where $i_{b2}[k+1], i_{b2}[k]$ can be calculated using $\phi[k]$ (already known) and $\phi[k+1]$ (predicted) based on the reduced order model (2). The error caused by power losses can be compensated using I_{comp} [28]:

$$I_{\text{comp}}[k] = i_{b2\_r}[k-1] - i_{b2}[k-1] \qquad (67)$$

where i_{b2} is indicated in Fig. 10 and is calculated using the reduced order model (2) (without power losses); i_{b2_r} is calculated using the the measured load current I_{load}, where the information of power losses is included:

$$i_{b2\_r}[k-1] = \frac{C_2}{T_s}(v_2[k] - v_2[k-1]) + I_{\text{load}}[k-1] \qquad (68)$$

Fig. 40 shows how to choose ϕ in the next switching cycle. In the control interval k to $k+1$, when $\phi[k+1]$ equals to $a - \Delta_f$, a and $a + \Delta_f$, the output voltage v_2 is predicted as $v_2^{(1)}[k+2]$, $v_2^{(2)}[k+2]$ and $v_2^{(3)}[k+2]$ respectively based on (2) and (66). As shown in Fig. 40, when $\phi[k+1] = a + \Delta_f$, the predicted output voltage $v_2^{(3)}[k+2]$ is the closest to V_2^*. This results in the smallest cost function defined in (65). Therefore, the value $a + \Delta_f$ is applied to ϕ at time instance $k+1$. In the next control interval, the same process is repeated. However, the moving discretized control set has changed and become $\{a, a + \Delta_f, a + 2\Delta_f\}$, centered at the previous working point $\phi[k+1] = a + \Delta_f$. In this control interval, $\phi[k+2] = a$ results in smallest cost function.

In the above example, $\mu = 3$ points are assessed in each switching cycle, larger value of μ can increase the transition dynamics, but it aggravates the computational burden to the real-time digital controller. Therefore, an adaptive step for ϕ is adopted instead of the finest search step Δ_f. Define the adaptive step Δ_{adp} as (70). The adaptive step Δ_{adp} changes with the deviation of the output voltage to the reference. When v_2 is far from the reference, Δ_{adp} grows large. In contrast, when v_2 equals to the reference, Δ_{adp} becomes Δ_f. Such that, the control accuracy remains.

$$V_\Delta = \begin{cases} |V_2^* - v_2[k]|, & |V_2^* - v_2[k]| < V_m \\ V_m, & |V_2^* - v_2[k]| > V_m \end{cases} \qquad (69)$$

$$\Delta_{adp} = \Delta_f(1 + \lambda V_\Delta^{\;2}), \qquad (70)$$

where V_m is the saturated voltage and λ is a coefficient determined according to the requirement of transition performance.

To provide damping and enhance the resistance to analogue to digital sampling noise in practice, the cost function can be modified as follows:

$$ct = \alpha_1 G_1 + \alpha_2 G_2, \qquad (71)$$

where

$$\begin{cases} G_1 = (V_2^* - v_2[k+2])^2 \\ G_2 = (v_2[k+2] - v_2[k])^2 \end{cases} \qquad (72)$$
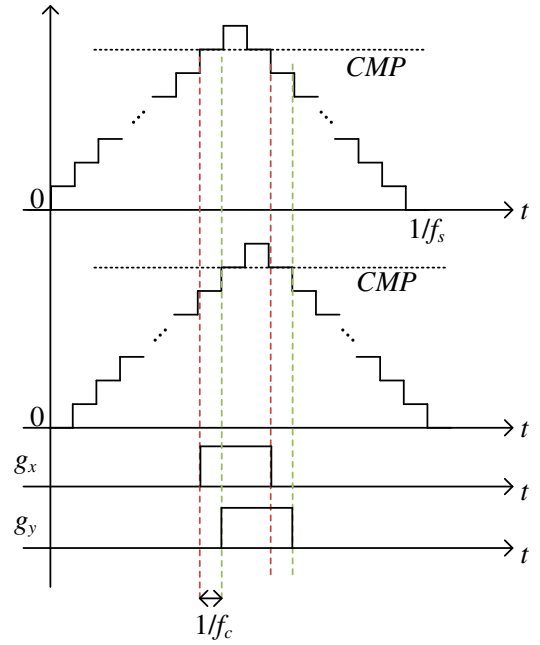
Fig. 39: Demonstration of the finest phase shift value in PWM modules [69].
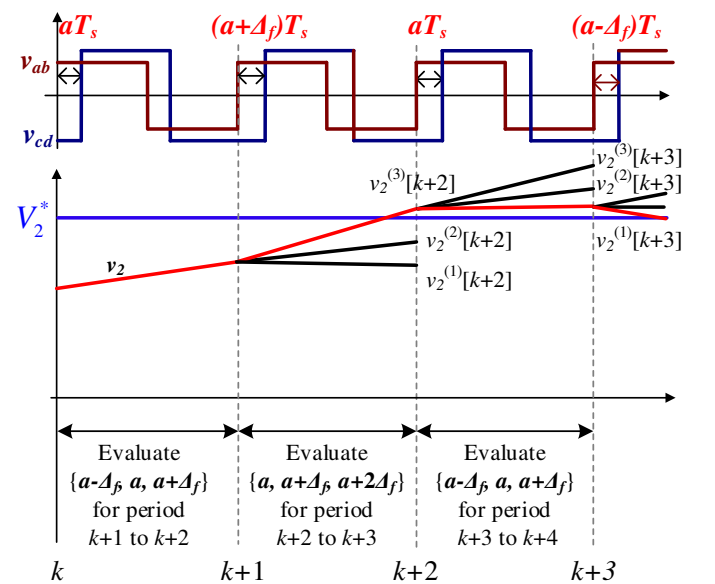
Fig. 40: Operating principle of MDCS-MPC and μ is set to be 3 for illustration [69].

The first term G_1 is responsible for regulation of the output voltage v_2 to reference value V_2^* while the second term G_2 takes charge of voltage deviation reduction. When v_2 is far from the reference value, G_1 plays a dominant role in the cost function. However, when v_2 reaches close to V_2^*, G_2 starts to take effect. G_2 puts constraint on variation of v_2. This essentially prevents v_2 from dithering due to analogue to digital sampling noise. G_2 also alleviates the oscillation during load transitions. More terms can be added to the cost function to achieve multiple control objectives [71].

The development of the analytical small signal model of

DAB converters with MDCS-MPC is infeasible. The small signal evaluation circuit in Figs. 14 and 15 are employed to obtain the frequency response plot of $G_{ro}(s)$ and $Z_o(s)$. The control parameters for MDCS-MPC is set as: $\alpha_1 = 1, \alpha_2 = 0.5, \mu = 11, \lambda = 1, V_m = 10V$. Fig. 35 shows the swept results for $G_{ro}(s)$ and $Z_o(s)$. In light of the observation of plots in Fig. 35, it can be concluded that the MDCS-MPC presents smaller output impedance compared to predictive current and feedback only approaches across the frequency range under test. As shown in Fig. 27, the MDCS-MPC has lower voltage overshoot under step change on load and output reference, compared to feedback-only or VDPC.The MDCS-MPC also features a transfer function $G_{ro}(s)$ which always stays below 0dB. The MDCS-MPS is also employed to control the DAB with TPS modulation [28].

H. Comparison of output voltage control methods

The above control methods are compared in this section. The control parameters are summarized in Table III. These parameters are chosen such that the open-loop of each method achieves 1.2kHz crossover frequency with $45°$ phase margin. Based on the theoretical transfer function or the bode plot, these PI parameters can be calculated.

TABLE III: Control parameters.

Control Methods	Control Parameters
Feedback only, Fig. 16	$k_{p1} = 0.0193, k_{i1} = 37.6$
Linerization, Fig. 19 [45]	$k_{p2} = 7.3155, k_{i2} = 1.425 \times 10^4$
OCFF, Fig. 22	$k_{p3} = 0.0193, k_{i3} = 37.6$
VDPC, Fig. 25 [48]	$k_{p4} = 38.524, k_{i4} = 1.068 \times 10^5$
DOBC, Fig. 28 [50]	$k_{p5} = 7.53 \times 10^3, k_{i5} = 1.37 \times 10^7$
FFCC, Fig. 30 [53]	$k_{p6} = 4.35, k_{i6} = 3.17 \times 10^4$
Predictive current, Fig. 34 [56]	$k_{p7} = 24.8, k_{i7} = 1.45 \times 10^5$
SMC, Fig. 36 [68]	$k_{p8} = 7.3155, k_{i8} = 1.425 \times 10^4$
MDCS-MPC [69]	$\alpha_1 = 1, \alpha_2 = 0.5, \mu = 11,$ $\lambda = 1, V_m = 10V$

Table IV compares these control methods in terms of implementation complexity, dynamic performance, robustness against parameter variation and implementation cost. The implementation cost include costs of voltage/current sensors and microprocessor computational power for method to be functioning. The required microprocessor computational power is related to the control method complexity. The high cost methods are those with high implementation complexity and 3 sensors. The low cost methods are those with low complexity and 1 sensors. The FFCC and MDCS-MPC have higher implementation cost compared to other control methods. The detailed remarks are given as below. Note that these remarks are only based on theoretical analysis and simulations, and are not validated using experimental results. Practical performance of these control methods can be different from that listed in Table IV.

- The feedback only control approach shows mediocre dynamic performance, however, it is easy to implement and requires only one transducer.

- The linerization control can transform the control loop into linear system and can counterbalance the influence of terminal voltage and load variation theoretically, however, its performance deteriorates when circuit parameters used in the control are different from the actual circuit parameters. Besides, the linearization is actually not required since the closed-loop bandwidth and output impedance of the feedback-only control almost does not vary with different output voltage or load conditions.

- OCFF control can significantly reduce the output impedance and present perfect load current disturbance rejection capability, however, its performance deteriorates quickly when there are parameter uncertainties. As shown in Fig. 24, when $L = 1.3L_0$, the output impedance of the OCFF control becomes the same as that of the feedback only control.

- The VDPC tries to solve parameter sensitivity problem of the OCFF control by using the PI output to estimate the phase shift. The biggest problem of the VDPC is the loop gain varies significantly under different load conditions. Under light load conditions, the bandwidth is too narrow and output impedance is too high, leading to poor performance on voltage tracking and load current disturbance rejection.

- The DOBC employs an observer to estimate the total disturbances and uncertainties, and corresponding compensation is generated by making use of the estimate. As a result, the DOBC shows much smaller output impedance compared with feedback-only control. The performance of the DOBC is not sensitive to the parameter variation. Besides, only one transducer is required.

- FFCC is essentially a peak current mode control method with feedforward compensation. The DAB with the FFCC control has small output impedance since the changes on output current or voltage can lead to immediate change at the inductor current. In the presence of the parameter tolerance, the performance of FFCC control degrades less significantly compared to the OCFF control. However, the FFCC control is susceptible to noise, especially when the DAB loses ZVS-on.

- The predictive current control can also improve the dynamic performance. Under the same control bandwidth, the output impedance of the predictive current control is lower than that of the feedback only control. This method may not be feasible for high frequency applications, since ac sampling and computation are required for each switching cycle.

- MDCS-MPC has similar ability in load disturbance rejection with the OCFF control. In the meantime, MDCS-MPC provides salient output voltage tracking performance. However, MDCS-MPC demands relatively heavy computation power which is a common issue as with other model predictive control. The control parameters such as weighting factors and the number of points calculated in one control cycle have a significant impact on the control performance. Inappropriate control parameters will cause system instability. Compared with the feedback-only control, the parameters are mainly selected

TABLE IV: Comparison of DAB control methods.

Control Methods	Implementation complexity	Dynamic performance	Robustness against parameter variation	Implementation cost	Other comments
Feedback only	Low	++	+++	Low, 1 sensor	
Feed-forward	Medium	++++	++	Medium, 3 sensors	
VDPC	Medium	+++	+	Medium, 3 sensors	Poor steady-state and dynamic performance under light load conditions
DOBC	Medium	++++	++++	Medium, 1 sensor	
FFCC	High	++++	+++	High, 3 sensors	Can be affected by the switching noise (similar to peak current mode control).
Predictive current control	Medium	++++	++	Medium, 3 sensors	Not suitable for high frequency applications.
SMC	Low	++	++	Low, 1 sensor	
MDCS-MPC	High	++++	++	High, 3 sensors	The control parameters have a significant impact on the control performance, these control parameters are chosen based on trial and error or the machine learning.

Note: **+ = Poor**; **++ = Average**; **+++ = Good**; **++++ = Excellent**

based on trial and error or the machine learning approach. This complicates the design.

- The methods with the lowest and highest computational reported complexity are the feedback only control and MDCS-MPC, respectively. According to [28], with the Texas Instruments TMS320F2837xD MCU, the computation time of the feedback only control and MDCS-MPC is $4.2\mu s$ and $18.6\mu s$, respectively. The computation times of other methods are between these two values.

IV. SOME PRACTICAL CONTROL ISSUES

This section surveys some practical control issues including dead time effect, phase drift and dc offset during dynamic transition.

1) Dead time effect: During the dead time period of a leg, the power devices turn off and the leg voltages (v_a, v_b in Fig. 41) only depend on the current direction. If the dead time is too long, the voltage may change polarity during this period [72]–[76]. Consider a DAB modulated using SPS, during the dead time of the primary side H-bridge, all the power devices are "OFF" as shown in Fig. 41, v_{ab} may change polarity if the dead time is too long, leading to undesirable voltage spikes, as shown in Fig. 42 [32] [76]. This phenomenon will bring electromagnetic interference (EMI) [72] and should be avoided by choosing a proper dead time.

The upper limit for the dead time to prevent the voltage spikes can be estimated assuming linear transformer behavior and ZVS-on transition. For a DAB modulated using SPS, the maximum dead time for the primary side device is [77]:

$$t_{dead.\,\max} = \frac{I_{sw} \cdot L}{V_1 + NV_2} \qquad (73)$$

where I_{sw} is the inductor current at the switching instant.

2) Phase drift: The actual phase shift can be different from the theoretical one given in (1). There are a few reasons for the phase drift. The first reason is the voltage drop on power devices and other components. Consider a DAB transfers positive power using SPS modulation as shown in Fig. 43
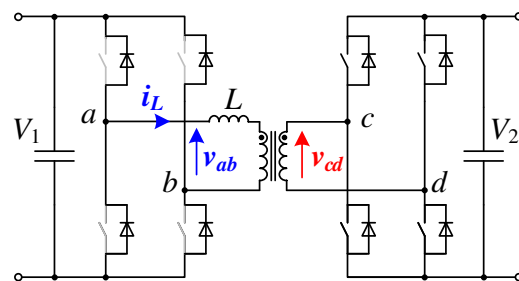
Fig. 41: Equivalent circuit of a DAB (modulated using SPS) during primary side H-bridge dead time.
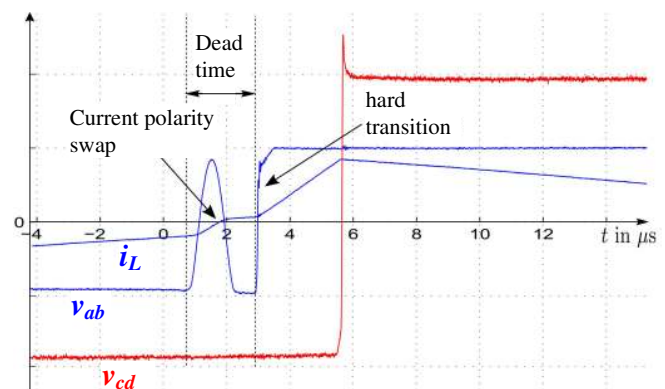
Fig. 42: Experimental waveforms: voltage change polarity during the dead time [76].

(a). When $t < T_h$, $v_{ab} = V_1 - i_L R_{eq}$, as shown in Fig. 43 (b), where R_{eq} is the equivalent resistances of the primary side; while $T_h < t < T_s$, $v_{ab} = -V_1 - i_L R_{eq}$. These voltage drops cause the equivalent phase of v_{ab} and v'_{cd} shift to the left and right respectively. In the case of Fig. 43, the given phase shift is $\phi < 0$, but the phase between the fundamental components of v_{ab} and v'_{cd} $\phi_{(1)} > 0$ and the power is transferred from left to right.
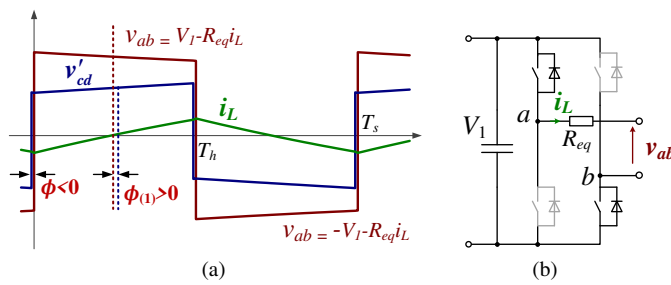
Fig. 43: Phase drift caused by voltage drop on components (a) waveforms, (b) equivalent circuit when $0 < t < T_h$.

Fig. 45: Inductor current (i_L) and magnetizing current (i_m) with and without steady state DC bias [78].

The second reason is the dead time. As explained in Fig. 41, during the dead time, the H-bridge output voltage depends on the current direction and its actual phase may vary from the given ϕ [72], [75], [76].

Another important reason for phase drift is the switching delay during the ZVS transition [77]. A large inductor current will shorten the ZVS transition period, and the phase drift is severest when the switching currents on the primary and secondary sides deviate considerably from each other as shown in Fig. 44.

Fig. 44: Phase drift caused by switching current difference on the primary and secondary sides [77].

3) DC magnetic flux bias: In practice, a DC magnetic flux bias will arise both in steady state and transient process for a DAB converter. As shown in Fig. 45, the steady state DC bias is caused by unmatched parameters of the circuit, like small discrepancy of the gate-drive signal, different turn on/off delay and unequal on-state resistance of the power devices; while the

Fig. 46: (a)DC offset during the load transient, (b) decay of dc offset over a time constant L/R_{eq} [79].

transient DC bias (Fig. 46) is caused by the temporary volt-second imbalance on inductor due to the update of phase shift ratio. The steady state DC bias will increase the conduction losses of the transformer and power devices and lead to loss of ZVS, whereas the transient DC bias may saturate magnetic cores of the transformer and inductor, leading to the failure of the converter in the end [78].

The simplest way to suppress the steady state DC magnetic flux bias is to include "dc-blocking capacitors" in series with the transformer winding, this will however increase the system volume and cost, especially in high voltage high power applications. This DC bias can also be eliminated by active controlling the inductor current. One of the prerequisites of this control is to accurately measure the steady state dc bias, the following measurement methods have been proposed:

- Digital sampling and averaging. Sample the inductor current several times each switching cycle and average the sampled values [81];
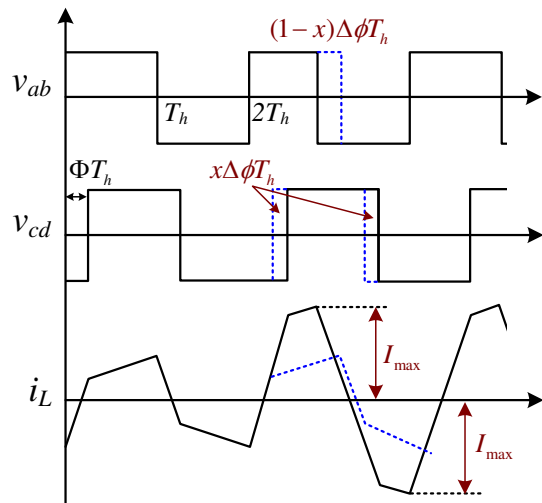
Fig. 47: A typical i_L dc offset suppression method for a DAB when $M < 1$, $x = 1/(1 + M)$ [80].

- Magnetic ear. An auxiliary circuit shares the magnetic path with the DAB transformer core and senses the flux bias using integrator circuit [82];
- Analog integration circuit. Primary and secondary side transformer currents are integrated using an analog integration circuit based on operational amplifier (op-amp) [78]. An active reset switch is added to periodically reset the integration circuit to avoid output offset caused by the internal bias current and voltage of the op-amp.

The measured dc bias is then used to regulate the duty cycle of primary and secondary side square voltages to eliminate the dc bias. The transfer function from duty cycle to the steady-state bias current as well as the controller design are detailed in [78].

The most common methods to suppress the transient dc offset in inductor current is to change the phase shift ratio (Φ to $\Phi + \Delta\phi$) by a two-step manner [80], [83]–[85]. Fig. 47 shows a typical example, and during the intermediate step the falling edge of v_{ab} shrinks $(1 - x)\Delta\phi T_h$, and v_{cd} shifts $x\Delta\phi T_h$, and the resultant i_L has no offset. To eliminate DC offset in both inductor current and transformer magnetizing current, duty cycles of v_{ab}, v_{cd} and their phase shifts have to be manipulated [79]. The two-step methods have been concluded, reviewed and compared in [86], and this method is extended to DAB converters using TPS [87].

Another method to suppress transient dc offset is to simply limit the peak inductor current [78]. When the inductor exceeds a preset threshold value, one of the H-bridges will change the output polarity ignoring phase shift command given by the controller. The peak current limit method in [78] is acceptable since the primary purpose of the transient dc offset suppression is to avoid magnetic components saturation. When the magnetic component saturation is avoided, the transient DC-bias will be settled down by the parasitic resistance as shown in Fig. 46 (b).

V. CONCLUSION AND FUTURE TREND

This work reviews the modeling and control for DAB dc-dc converter. Three types of modeling techniques, i.e. reduced-order model, generalized average model and discrete time model, are comprehensively introduced and critically compared based on simulation results. The model accuracy and complexity of each method are summarized in Table II. The reduced order model has the best overall performance due to its simplicity and good conformity to the simulation results. The reduced order model is of first order and inductance does not affect the DAB dynamic performance, similar to that of the traditional dc-dc converter operating in DCM. For high frequency DAB where the ZVS intervals have significant impact on dynamics, the discrete-time model may be a better choice.

Different control methods including feedback control, linearization control, feedforward plus feedback, disturbance observer based control (DOBC), feedforward current control (FFCC), model predictive current control, sliding mode control and moving discretized control set model predictive control (MDCS-MPC) are reviewed and compared. The closed-loop control-to-output $G_{ro}(s)$ and output impedance $Z_o(s)$ are selected as the metrics of the ability in voltage tracking and the load disturbance rejection performance. Table IV compares the performance of these control methods. Detailed remarks are also provided at the end of Section III. The DOBC shows excellent dynamic performance, better than the feedback only control. Besides, the DOBC is not sensitive to the parameter variations and only requires 1 transducer. MDCS-MPC, FFCC and more predictive current control also show excellent dynamic performance. However, these methods require 3 transducers. Besides, the control parameters of MDCS-MPC should be chosen based on trial-and-error or the machine learning. The FFCC can be affected by the switching noise (similar to peak current mode control). The predictive current control is not suitable for high frequency applications and is sensitive to parameter variation.

Practical control issues including dead time effect, phase drift and DC magnetic flux bias are also reviewed. The causes of these issues are comprehensively explained. The dead time effect can be avoided by choosing proper dead time. Phase drift can be caused by the voltage drop on components, dead time and switching delay during the ZVS transitions. Integral term should always be included in the control loop to compensate the phase drift. In terms of DC magnetic flux bias, the steady state dc bias can be suppressed using dc-blocking capacitors or active control of inductor current. The transient dc bias can be suppressed by changing phase shift ratio in two steps or by simply limiting the peak current during the transient period.

With the development of advanced modulation methods and wide adoption of wide bandgap (WBG) devices, there are several new challenges in modeling and control DAB converters. Firstly, there is a research gap on how to apply these control methods to DAB in conjunction with advanced modulations. The existing control methods are mostly for DAB with single phase shift (SPS). However, more and more research proposes

advanced modulations for DABs, such as dual phase shift (DPS), triple phase shift (TPS) or frequency modulation (FM), where either the duty cycles or frequencies of the square voltages are regulated. These advanced modulation methods can effectively suppress circulating current and expand ZVS-on region. To apply these advanced modulation methods in practice, it is necessary to build the models and coordinate the existing control methods with these modulations.

Secondly, for DAB with WBG devices, the sampling and control delays as well as the ZVS transition can occupy a considerable percentage of the overall microprocessor calculation period [35], [36]. Besides, the high dv/dt introduced by WBG devices can lead to inductor current oscillations and control instability [88], and the zero-voltage-switching (ZVS) of Gallium Nitride (GaN) devices can be affected by transformer parasitic capacitance [89]. To face these challenges, more detailed circuit model is required for these applications.

Thirdly, only resistive load is considered in evaluating the control methods, however, there are many other types of loads, such as constant power load (CPL) and pulsed power load (PPL). A typical CPL is the tightly regulated power electronics load, which exhibits negative incremental impedance characteristics [90]. The CPLs decrease the system damping. On the other hand, PPLs draw a large amount of power in a very short period, resulting in voltage sags. PPL is common in onboard microgrids like more electric aircrafts, electric ships or fast EV charging stations [90]. These two types of loads can push the system more easily beyond its safe operating margins compared to resistive loads [69], [90]. It is thus necessary to evaluate the DAB control methods under CPLs and PPLs to verify their performance in the most challenging scenarios. Other advanced control methods such as backstepping [90], [91], passivity-based controllers [92], intelligent control [93] can also be applied to control DAB with CPLs and PPLs.

REFERENCES

[1] T. Dragičević, X. Lu, J. C. Vasquez, and J. M. Guerrero, "Dc microgrids—part i: A review of control strategies and stabilization techniques," *IEEE Transactions on Power Electronics*, vol. 31, no. 7, pp. 4876–4891, July 2016.

[2] D. Boroyevich, I. Cvetković, D. Dong, R. Burgos, F. Wang, and F. Lee, "Future electronic power distribution systems a contemplative view," in *2010 12th International Conference on Optimization of Electrical and Electronic Equipment*, May 2010, pp. 1369–1380.

[3] Y. Gu, "Distributed peer-to-peer control for renewable power generation dc microgrid," Ph.D. dissertation, Zhejiang University, Hangzhou, Jul. 2015. [Online]. Available: https://www.cnki.net/

[4] B. Zhao, Q. Song, W. Liu, and Y. Sun, "Overview of dual-active-bridge isolated bidirectional dc-dc converter for high-frequency-link power-conversion system," *IEEE Transactions on Power Electronics*, vol. 29, no. 8, pp. 4091–4106, Aug 2014.

[5] R. W. D. Doncker, D. M. Divan, and M. H. Kheraluwala, "A three-phase soft-switched high power density dc/dc converter for high power applications," in *Conference Record of the 1988 IEEE Industry Applications Society Annual Meeting*, Oct 1988, pp. 796–805 vol.1.

[6] R. W. A. A. D. Doncker, D. M. Divan, and M. H. Kheraluwala, "A three-phase soft-switched high-power-density dc/dc converter for high-power applications," *IEEE Transactions on Industry Applications*, vol. 27, no. 1, pp. 63–73, Jan 1991.

[7] S. Shao, H. Chen, X. Wu, J. Zhang, and K. Sheng, "Circulating current and zvs-on of a dual active bridge dc-dc converter: A review," *IEEE Access*, vol. 7, pp. 50 561–50 572, 2019.

[8] A. Q. Huang, M. L. Crow, G. T. Heydt, J. P. Zheng, and S. J. Dale, "The future renewable electric energy delivery and management (freedm) system: The energy internet," *Proceedings of the IEEE*, vol. 99, no. 1, pp. 133–148, Jan 2011.

[9] B. Zhao, Q. Song, J. Li, and W. Liu, "A modular multilevel dc-link front-to-front dc solid-state transformer based on high-frequency dual active phase shift for hvdc grid integration," *IEEE Transactions on Industrial Electronics*, vol. 64, no. 11, pp. 8919–8927, Nov 2017.

[10] S. Shao, M. Jiang, J. Zhang, and X. Wu, "A capacitor voltage balancing method for a modular multilevel dc transformer for dc distribution system," *IEEE Transactions on Power Electronics*, vol. 33, no. 4, pp. 3002–3011, April 2018.

[11] D. Dujic, C. Zhao, A. Mester, J. K. Steinke, M. Weiss, S. Lewdeni-Schmid, T. Chaudhuri, and P. Stefanutti, "Power electronic traction transformer-low voltage prototype," *IEEE Transactions on Power Electronics*, vol. 28, no. 12, pp. 5522–5534, Dec 2013.

[12] C. Zhao, D. Dujic, A. Mester, J. K. Steinke, M. Weiss, S. Lewdeni-Schmid, T. Chaudhuri, and P. Stefanutti, "Power electronic traction transformer-medium voltage prototype," *IEEE Transactions on Industrial Electronics*, vol. 61, no. 7, pp. 3257–3268, July 2014.

[13] L. Xue, Z. Shen, D. Boroyevich, P. Mattavelli, and D. Diaz, "Dual active bridge-based battery charger for plug-in hybrid electric vehicle with charging current containing low frequency ripple," *IEEE Transactions on Power Electronics*, vol. 30, no. 12, pp. 7299–7307, Dec 2015.

[14] J. Lu, K. Bai, A. R. Taylor, G. Liu, A. Brown, P. M. Johnson, and M. McAmmond, "A modular-designed three-phase high-efficiency high-power-density ev battery charger using dual/triple-phase-shift control," *IEEE Transactions on Power Electronics*, vol. 33, no. 9, pp. 8091–8100, Sept 2018.

[15] Z. Zhang, J. Huang, and Y. Xiao, "Gan-based 1-mhz partial parallel dual active bridge converter with integrated magnetics," *IEEE Transactions on Industrial Electronics*, vol. 68, no. 8, pp. 6729–6738, 2021.

[16] W. Xu, R. y. Yu, Z. Guo, and A. Q. Huang, "Design of 1500v/200kw 99.6efficiency dual active bridge converters based on 1700v sic power mosfet module," in *2020 IEEE Energy Conversion Congress and Exposition (ECCE)*, 2020, pp. 6000–6007.

[17] W. Xu, Z. Guo, S. M. Tayebi, S. Rajendran, A. Sun, R. Yu, and A. Q. Huang, "Hardware design and demonstration of a 100kw, 99half bridge converter based on 1700v sic power mosfet," in *2020 IEEE Applied Power Electronics Conference and Exposition (APEC)*, 2020, pp. 1367–1373.

[18] S. Inoue and H. Akagi, "A bidirectional dc-dc converter for an energy storage system with galvanic isolation," *IEEE Transactions on Power Electronics*, vol. 22, no. 6, pp. 2299–2306, Nov 2007.

[19] C. Gammeter, F. Krismer, and J. W. Kolar, "Comprehensive conceptualization, design, and experimental verification of a weight-optimized all-sic 2 kv/700 v dab for an airborne wind turbine," *IEEE Journal of Emerging and Selected Topics in Power Electronics*, vol. 4, no. 2, pp. 638–656, June 2016.

[20] Y. W. Cho, W. J. Cha, J. M. Kwon, and B. H. Kwon, "High-efficiency bidirectional dab inverter using a novel hybrid modulation for stand-alone power generating system with low input voltage," *IEEE Transactions on Power Electronics*, vol. 31, no. 6, pp. 4138–4147, June 2016.

[21] H. Y. Kanaan, M. Caron, and K. Al-Haddad, "Design and implementation of a two-stage grid-connected high efficiency power load emulator," *IEEE Transactions on Power Electronics*, vol. 29, no. 8, pp. 3997–4006, Aug 2014.

[22] N. Hou and Y. W. Li, "Overview and comparison of modulation and control strategies for a nonresonant single-phase dual-active-bridge dc–dc converter," *IEEE Transactions on Power Electronics*, vol. 35, no. 3, pp. 3148–3172, March 2020.

[23] A. S. Babokany, M. Jabbari, G. Shahgholian, and M. Mahdavian, "A review of bidirectional dual active bridge converter," in *2012 9th International Conference on Electrical Engineering/Electronics, Computer, Telecommunications and Information Technology*, May 2012, pp. 1–4.

[24] R. W. Erickson and D. Maksimovic, *Fundamentals of power electronics*. Springer Science & Business Media, 2007.

[25] A. R. Alonso, J. Sebastian, D. G. Lamar, M. M. Hernando, and A. Vazquez, "An overall study of a dual active bridge for bidirectional dc/dc conversion," in *2010 IEEE Energy Conversion Congress and Exposition*, Sept 2010, pp. 1129–1135.

[26] H. Bai, C. Mi, C. Wang, and S. Gargies, "The dynamic model and hybrid phase-shift control of a dual-active-bridge converter," in *2008 34th Annual Conference of IEEE Industrial Electronics*, Nov 2008, pp. 2840–2845.

[27] H. Bai, Z. Nie, and C. C. Mi, "Experimental comparison of traditional phase-shift, dual-phase-shift, and model-based control of isolated bidi-

rectional dc-dc converters," *IEEE Transactions on Power Electronics*, vol. 25, no. 6, pp. 1444–1449, June 2010.

[28] L. Chen, L. Lin, S. Shao, F. Gao, Z. Wang, P. W. Wheeler, and T. Dragičević, "Moving discretized control set model-predictive control for dual-active bridge with the triple-phase shift," *IEEE Transactions on Power Electronics*, vol. 35, no. 8, pp. 8624–8637, 2020.

[29] K. Zhang, Z. Shan, and J. Jatskevich, "Large- and small-signal average-value modeling of dual-active-bridge dc-dc converter considering power losses," *IEEE Transactions on Power Electronics*, vol. 32, no. 3, pp. 1964–1974, March 2017.

[30] V. A. Caliskan, O. C. Verghese, and A. M. Stankovic, "Multifrequency averaging of dc/dc converters," *IEEE Transactions on Power Electronics*, vol. 14, no. 1, pp. 124–133, Jan 1999.

[31] H. Qin and J. W. Kimball, "Generalized average modeling of dual active bridge dc-dc converter," *IEEE Transactions on Power Electronics*, vol. 27, no. 4, pp. 2078–2084, April 2012.

[32] D. Segaran, D. G. Holmes, and B. P. McGrath, "Enhanced load step response for a bidirectional dc-dc converter," *IEEE Transactions on Power Electronics*, vol. 28, no. 1, pp. 371–379, Jan 2013.

[33] C. Zhao, S. D. Round, and J. W. Kolar, "Full-order averaging modelling of zero-voltage-switching phase-shift bidirectional dc-dc converters," *IET Power Electronics*, vol. 3, no. 3, pp. 400–410, May 2010.

[34] F. Krismer and J. W. Kolar, "Accurate small-signal model for the digital control of an automotive bidirectional dual active bridge," *IEEE Transactions on Power Electronics*, vol. 24, no. 12, pp. 2756–2768, Dec 2009.

[35] D. Costinett, R. Zane, and D. Maksimović, "Discrete-time small-signal modeling of a 1 mhz efficiency-optimized dual active bridge converter with varying load," in *2012 IEEE 13th Workshop on Control and Modeling for Power Electronics (COMPEL)*, June 2012, pp. 1–7.

[36] D. Costinett, "Reduced order discrete time modeling of zvs transition dynamics in the dual active bridge converter," in *2015 IEEE Applied Power Electronics Conference and Exposition (APEC)*, March 2015, pp. 365–370.

[37] L. Shi, W. Lei, Z. Li, J. Huang, Y. Cui, and Y. Wang, "Bilinear discrete-time modeling and stability analysis of the digitally controlled dual active bridge converter," *IEEE Transactions on Power Electronics*, vol. 32, no. 11, pp. 8787–8799, Nov 2017.

[38] D. Maksimovic and R. Zane, "Small-signal discrete-time modeling of digitally controlled pwm converters," *IEEE Transactions on Power Electronics*, vol. 22, no. 6, pp. 2552–2556, Nov 2007.

[39] S. Shao, M. Jiang, W. Ye, Y. Li, J. Zhang, and K. Sheng, "Optimal phase-shift control to minimize reactive power for a dual active bridge dc–dc converter," *IEEE Transactions on Power Electronics*, vol. 34, no. 10, pp. 10 193–10 205, Oct 2019.

[40] J. Huang, Y. Wang, Z. Li, and W. Lei, "Unified triple-phase-shift control to minimize current stress and achieve full soft-switching of isolated bidirectional dc–dc converter," *IEEE Transactions on Industrial Electronics*, vol. 63, no. 7, pp. 4169–4179, July 2016.

[41] G. Xu, D. Sha, J. Zhang, and X. Liao, "Unified boundary trapezoidal modulation control utilizing fixed duty cycle compensation and magnetizing current design for dual active bridge dc–dc converter," *IEEE Transactions on Power Electronics*, vol. 32, no. 3, pp. 2243–2252, March 2017.

[42] G. G. Oggier, G. O. GarcÍa, and A. R. Oliva, "Switching control strategy to minimize dual active bridge converter losses," *IEEE Transactions on Power Electronics*, vol. 24, no. 7, pp. 1826–1838, July 2009.

[43] M. N. Kheraluwala, R. W. Gascoigne, D. M. Divan, and E. D. Baumann, "Performance characterization of a high-power dual active bridge dc-to-dc converter," *IEEE Transactions on Industry Applications*, vol. 28, no. 6, pp. 1294–1301, Nov 1992.

[44] H. Qin and J. W. Kimball, "Closed-loop control of dc-dc dual-active-bridge converters driving single-phase inverters," *IEEE Transactions on Power Electronics*, vol. 29, no. 2, pp. 1006–1017, Feb 2014.

[45] A. Tong, L. Hang, H. S. Chung, G. Li, K. Wang, and Y. He, "Using sampled-data modeling method to derive equivalent circuit and linearized control method for dual-active-bridge converter," *IEEE Journal of Emerging and Selected Topics in Power Electronics*, pp. 1–1, 2019.

[46] F. An, W. Song, K. Yang, N. Hou, and J. Ma, "Improved dynamic performance of dual active bridge dc–dc converters using mpc scheme," *IET Power Electronics*, vol. 11, no. 11, pp. 1756–1765, 2018.

[47] W. Zhao, X. Zhang, S. Gao, and M. Ma, "Improved model-based phase-shift control for fast dynamic response of dual active bridge dc/dc converters," *IEEE Journal of Emerging and Selected Topics in Power Electronics*, pp. 1–1, 2020.

[48] W. Song, N. Hou, and M. Wu, "Virtual direct power control scheme of dual active bridge dc-dc converters for fast dynamic response," *IEEE Transactions on Power Electronics*, vol. 33, no. 2, pp. 1750–1759, Feb 2018.

[49] W. Chen, J. Yang, L. Guo, and S. Li, "Disturbance-observer-based control and related methods—an overview," *IEEE Transactions on Industrial Electronics*, vol. 63, no. 2, pp. 1083–1095, 2016.

[50] M. Ali, M. Yaqoob, L. Cao, and K. H. Loo, "Disturbance-observer-based dc-bus voltage control for ripple mitigation and improved dynamic response in two-stage single-phase inverter system," *IEEE Transactions on Industrial Electronics*, vol. 66, no. 9, pp. 6836–6845, 2019.

[51] F. Xiong, J. Wu, Z. Liu, and L. Hao, "Current sensorless control for dual active bridge dc-dc converter with estimated load-current feedforward," *IEEE Transactions on Power Electronics*, vol. 33, no. 4, pp. 3552–3566, April 2018.

[52] Y. Wu, M. Mahmud, Y. Zhao, and H. A. Mantooth, "Uncertainty and disturbance estimator based robust tracking control for dual-active-bridge converters," *IEEE Transactions on Transportation Electrification*, pp. 1–1, 2020.

[53] Z. Shan, J. Jatskevich, H. H. Iu, and T. Fernando, "Simplified load-feedforward control design for dual-active-bridge converters with current-mode modulation," *IEEE Journal of Emerging and Selected Topics in Power Electronics*, vol. 6, no. 4, pp. 2073–2085, Dec 2018.

[54] S. Tan, P. Lin, C. Hu, L. Chen, and D. Xu, "Interleaved flyback micro-inverter with sic mosfet," in *2014 International Power Electronics and Application Conference and Exposition*, Nov 2014, pp. 285–290.

[55] L. Dixon, "Average current mode control of switching power supplies," in *Unitrode Power Supply Design Seminar Handbook*. Unitrode Corporation, 1990, pp. 5–1.

[56] S. Dutta, S. Hazra, and S. Bhattacharya, "A digital predictive current-mode controller for a single-phase high-frequency transformer-isolated dual-active bridge dc-to-dc converter," *IEEE Transactions on Industrial Electronics*, vol. 63, no. 9, pp. 5943–5952, Sep. 2016.

[57] S. Dutta, S. Bhattacharya, and M. Chandorkar, "A novel predictive phase shift controller for bidirectional isolated dc to dc converter for high power applications," in *2012 IEEE Energy Conversion Congress and Exposition (ECCE)*, Sep. 2012, pp. 418–423.

[58] L. Zhu, A. R. Taylor, G. Liu, and K. Bai, "A multiple-phase-shift control for a sic-based ev charger to optimize the light-load efficiency, current stress, and power quality," *IEEE Journal of Emerging and Selected Topics in Power Electronics*, vol. 6, no. 4, pp. 2262–2272, Dec 2018.

[59] S.-C. Tan, Y.-M. Lai, and C.-K. Tse, *Sliding mode control of switching power converters: techniques and implementation*. CRC press, 2011.

[60] A. R. Brown and R. D. Middlebrook, "Sampled-data modeling of switching regulators," in *1981 IEEE Power Electronics Specialists Conference*, June 1981, pp. 349–369.

[61] D. C. Hamill, J. H. B. Deane, and D. J. Jefferies, "Modeling of chaotic dc-dc converters by iterated nonlinear mappings," *IEEE Transactions on Power Electronics*, vol. 7, no. 1, pp. 25–36, Jan 1992.

[62] V. Utkin, J. Guldner, and J. Shi, *Sliding mode control in electromechanical systems*. CRC press, 2009.

[63] Y. Jeung and D. Lee, "Voltage and current regulations of bidirectional isolated dual-active-bridge dc–dc converters based on a double-integral sliding mode control," *IEEE Transactions on Power Electronics*, vol. 34, no. 7, pp. 6937–6946, July 2019.

[64] K. Li, Y. Yang, S. Tan, and R. S. Hui, "Sliding-mode-based direct power control of dual-active-bridge dc-dc converters," in *2019 IEEE Applied Power Electronics Conference and Exposition (APEC)*, March 2019, pp. 188–192.

[65] P. Mattavelli, L. Rossetto, G. Spiazzi, and P. Tenti, "General-purpose sliding-mode controller for dc/dc converter applications," in *Proceedings of IEEE Power Electronics Specialist Conference - PESC '93*, June 1993, pp. 609–615.

[66] V. M. Nguyen and C. Q. Lee, "Indirect implementations of sliding-mode control law in buck-type converters," in *Proceedings of Applied Power Electronics Conference. APEC '96*, vol. 1, March 1996, pp. 111–115 vol.1.

[67] S. Tan, Y. M. Lai, and C. K. Tse, "Indirect sliding mode control of power converters via double integral sliding surface," *IEEE Transactions on Power Electronics*, vol. 23, no. 2, pp. 600–611, March 2008.

[68] K. Li, Y. Yang, S. Tan, and R. S. Hui, "Sliding-mode-based direct power control of dual-active-bridge dc-dc converters," in *2019 IEEE Applied Power Electronics Conference and Exposition (APEC)*, March 2019, pp. 188–192.

[69] L. Chen, S. Shao, Q. Xiao, L. Tarisciotti, T. Dragicevic, and P. Wheeler, "Model-predictive-control for dual-active-bridge converters supplying pulsed power loads in naval dc microgrids," *IEEE Transactions on Power Electronics*, pp. 1–1, 2019.

[70] L. Chen, L. Tarisciotti, A. Costabeber, P. Wheeler, and P. Zanchetta, "Model predictive control for isolated dc/dc power converters with transformer peak current shaving," in *2018 IEEE Energy Conversion Congress and Exposition (ECCE)*, Sep. 2018, pp. 5954–5960.

[71] L. Chen, F. Gao, K. Shen, Z. Wang, L. Tarisciotti, P. Wheeler, and T. Dragičević, "Predictive control based dc microgrid stabilization with the dual active bridge converter," *IEEE Transactions on Industrial Electronics*, vol. 67, no. 10, pp. 8944–8956, 2020.

[72] H. Bai, C. C. Mi, and S. Gargies, "The short-time-scale transient processes in high-voltage and high-power isolated bidirectional dc-dc converters," *IEEE Transactions on Power Electronics*, vol. 23, no. 6, pp. 2648–2656, Nov 2008.

[73] J. Li, Z. Chen, Z. Shen, P. Mattavelli, J. Liu, and D. Boroyevich, "An adaptive dead-time control scheme for high-switching-frequency dual-active-bridge converter," in *2012 Twenty-Seventh Annual IEEE Applied Power Electronics Conference and Exposition (APEC)*, Feb 2012, pp. 1355–1361.

[74] D. Costinett, R. Zane, and D. Maksimovic, "Automatic voltage and dead time control for efficiency optimization in a dual active bridge converter," in *2012 Twenty-Seventh Annual IEEE Applied Power Electronics Conference and Exposition (APEC)*, Feb 2012, pp. 1104–1111.

[75] B. Zhao, Q. Song, W. Liu, and Y. Sun, "Dead-time effect of the high-frequency isolated bidirectional full-bridge dc-dc converter: Comprehensive theoretical analysis and experimental verification," *IEEE Transactions on Power Electronics*, vol. 29, no. 4, pp. 1667–1680, April 2014.

[76] J. Riedel, D. G. Holmes, B. P. McGrath, and C. Teixeira, "Zvs soft switching boundaries for dual active bridge dc-dc converters using frequency domain analysis," *IEEE Transactions on Power Electronics*, vol. 32, no. 4, pp. 3166–3179, April 2017.

[77] J. Hiltunen, V. Väisänen, R. Juntunen, and P. Silventoinen, "Variable-frequency phase shift modulation of a dual active bridge converter," *IEEE Transactions on Power Electronics*, vol. 30, no. 12, pp. 7138–7148, Dec 2015.

[78] B. Zhang, S. Shao, L. Chen, X. Wu, and J. Zhang, "Steady state and transient dc magnetic flux bias suppression methods for a dual active bridge converter," *IEEE Journal of Emerging and Selected Topics in Power Electronics*, pp. 1–1, 2019.

[79] K. Takagi and H. Fujita, "Dynamic control and performance of a dual-active-bridge dc–dc converter," *IEEE Transactions on Power Electronics*, pp. 1–1, 2017.

[80] X. Li and Y. F. Li, "An optimized phase-shift modulation for fast transient response in a dual-active-bridge converter," *IEEE Transactions on Power Electronics*, vol. 29, no. 6, pp. 2661–2665, June 2014.

[81] S. Dutta and S. Bhattacharya, "A method to measure the dc bias in high frequency isolation transformer of the dual active bridge dc to dc converter and its removal using current injection and pwm switching," in *2014 IEEE Energy Conversion Congress and Exposition (ECCE)*, Sep. 2014, pp. 1134–1139.

[82] G. Ortiz, L. Fässler, J. W. Kolar, and O. Apeldoorn, "Flux balancing of isolation transformers and application of "the magnetic ear" for closed-loop volt–second compensation," *IEEE Transactions on Power Electronics*, vol. 29, no. 8, pp. 4078–4090, Aug 2014.

[83] S. P. Engel, N. Soltau, H. Stagge, and R. W. D. Doncker, "Dynamic and balanced control of three-phase high-power dual-active bridge dc-dc converters in dc-grid applications," *IEEE Transactions on Power Electronics*, vol. 28, no. 4, pp. 1880–1889, April 2013.

[84] B. Zhao, Q. Song, W. Liu, and Y. Zhao, "Transient dc bias and current impact effects of high-frequency-isolated bidirectional dc-dc converter in practice," *IEEE Transactions on Power Electronics*, vol. 31, no. 4, pp. 3203–3216, April 2016.

[85] S. T. Lin, X. Li, C. Sun, and Y. Tang, "Fast transient control for power adjustment in a dual-active-bridge converter," *Electronics Letters*, vol. 53, no. 16, pp. 1130–1132, 2017.

[86] Y. Tang, X. Li, S. Zhou, C. Sun, and G. Chen, "Comprehensive study of fast load modulation with volt-second balance in a dual-active-bridge converter," *IET Power Electronics*, vol. 12, no. 6, pp. 1357–1367, 2019.

[87] C. Sun, X. Li, and S. Zhou, "Transient current control for a step load change in a dual-active-bridge converter," *Electronics Letters*, vol. 54, no. 22, pp. 1290–1292, 2018.

[88] B. Cui, H. Shi, Q. Sun, X. Tang, L. Hong, and B. Zhao, "A novel analysis, design, and optimal methodology of high-frequency oscillation for dual active bridge converters with wbg switching devices and nanocrystalline transformer cores," *IEEE Transactions on Power Electronics*, vol. 36, no. 7, pp. 7665–7678, 2021.

[89] Y. Xiao, Z. Zhang, M. A. E. Andersen, and K. Sun, "Impact on zvs operation by splitting inductance to both sides of transformer for 1- mhz gan based dab converter," *IEEE Transactions on Power Electronics*, vol. 35, no. 11, pp. 11 988–12 002, 2020.

[90] Q. Xu, N. Vafamand, L. Chen, T. Dragičević, L. Xie, and F. Blaabjerg, "Review on advanced control technologies for bidirectional dc/dc converters in dc microgrids," *IEEE Journal of Emerging and Selected Topics in Power Electronics*, vol. 9, no. 2, pp. 1205–1221, 2021.

[91] S. Yousefizadeh, J. D. Bendtsen, N. Vafamand, M. H. Khooban, F. Blaabjerg, and T. Dragičević, "Tracking control for a dc microgrid feeding uncertain loads in more electric aircraft: Adaptive backstepping approach," *IEEE Transactions on Industrial Electronics*, vol. 66, no. 7, pp. 5644–5652, 2019.

[92] J. Zeng, Z. Zhang, and W. Qiao, "An interconnection and damping assignment passivity-based controller for a dc–dc boost converter with a constant power load," *IEEE Transactions on Industry Applications*, vol. 50, no. 4, pp. 2314–2322, 2014.

[93] N. Chettibi, A. Mellit, G. Sulligoi, and A. Massi Pavan, "Adaptive neural network-based control of a hybrid ac/dc microgrid," *IEEE Transactions on Smart Grid*, vol. 9, no. 3, pp. 1667–1679, 2018.

Shuai Shao (M'17) received the B.S. degree from Zhejiang University, China, in 2010, and the Ph.D. degree in electrical and electronic engineering from the University of Nottingham, U.K., in 2015.

In 2015, he joined the College of Electrical Engineering, Zhejiang University, as a lecturer. In Jan. 2020, he was promoted as an associate professor. His research interests include solid-state transformers, bidirectional dc-dc converters, and fault detection in power converters. He has published more than 40 peer-reviewed journal and conference papers. He served as a Guest Associate Editor for IEEE Journal of Emerging and Selected Topics in Power Electronics and CES Transactions on Electrical Machines and Systems.

Linglin Chen received the M.Sc. degree in electrical engineering from Zhejiang University, Hangzhou, China, in 2016 and the Ph.D degree in electrical and electronics engineering from the University of Nottingham, Nottingham, U.K., in 2020. From 2018 to 2019, he was a Visiting Scholar with the Department of Energy Technology, Aalborg University, Aalborg, Denmark. From 2019 to 2020, he was a Visiting Scholar with the Key Laboratory of Control of Power Transmission and Transformation, Shanghai Jiao Tong University, Shanghai, China. He joined Digital Power Huawei Techonologies in 2020, and he is currently with Hisillicon of the same company. His interests include HJT TOPon PV materials, SiC&GaN device&gate driver, PV optimizer&string inverter, telecom&server rectifier, USB&PD charger, OBC etc.

Zhenyu Shan (M'14) received the B.Eng. and M.Eng. degrees in control engineering from Beijing Jiaotong University, Beijing, China in 2007 and 2009, respectively, and the Ph.D. degree in electrical engineering from Hong Kong Polytechnic University in 2013. He was a visiting student at University of Illinois at Urbana-Champaign, U.S. from March to June in 2013.

He was a Postdoctoral Research Fellow at University of British Columbia, Vancouver, Canada during November 2013 to June 2016. He was selected into Beijing Sea Poly Overseas Young Talent Program at North China University of Technology, Beijing, China from 2017 to 2019. He is currently an Assistant Professor and Associate Head of the Department of Electrical Engineering, Beihang University, Beijing, China. Dr. Shan is a Professional Committee Member of China Power Supply Society, and serves as a Reviewer for various IEEE transactions and other international journals on electrical and electronic engineering. His research interests include modeling and nonlinear control of power electronic circuits.

Fei Gao (M'18) received his Ph.D. degree in Electrical Engineering from the Power Electronics, Machines, and Control (PEMC) Research Group, University of Nottingham, Nottingham, UK, in 2016. From Mar. 2010 to Sep. 2012, he has worked in Jiangsu Electric Power Research Institute, Nanjing, State Grid Corporation of China. From 2016 to 2019, he has been with Department of Engineering Science, University of Oxford, UK as a postdoctoral researcher. Since July 2019 he joined Shanghai Jiao Tong University as an associate professor. His current research interests include modelling, control, power management and stability of microgrids and more electric transportation systems. Dr. Gao won the European Union Clean Sky Best PhD Award in 2017 and IET Control & Automation Runner Up PhD Award in 2018.

Hui Chen was born in Zhejiang Province, China, in 1988. She received the B.S. degree and Ph.D. degree in electrical engineering from Zhejiang University, Hangzhou, China, in 2010 and 2015 respectively. She is now with Zhejiang University City College, Hangzhou, China.

Her current research interests include high-efficiency dc-dc converters and topology research.

Deshang Sha (M'09-SM'17) received his B.S. from the Luoyang Institute of Technology, Luoyang, China, in 1998, his M.S. from the Nanjing University of Aeronautics and Astronautics (NUAA), Nanjing, China in 2001, and his Ph.D. from the Institute of Electrical Engineering, Chinese Academy of Sciences, Beijing, China, in 2005, all in Electrical Engineering. Since 2008, he has been with the School of Automation, Beijing Institute of Technology (BIT), Beijing, China, where he is currently a tenured Associate Professor. From 2012 to 2013, he was a Visiting Scholar with the Future Energy Electronics Center (FEEC), Virginia Polytechnic Institute and State University, Blacksburg, Virginia. He has authored over 100 papers and three books. His current research interests include the modeling and control of power converters, high-efficiency power conversion.

Tomislav Dragičević (S'09-M'13-SM'17) received the M.Sc. and the industrial Ph.D. degrees in Electrical Engineering from the Faculty of Electrical Engineering, University of Zagreb, Croatia, in 2009 and 2013, respectively. From 2013 until 2016 he has been a Postdoctoral researcher at Aalborg University, Denmark. From 2016 until 2020 he was an Associate Professor at Aalborg University, Denmark. Currently, he is a Professor at the Technical University of Denmark. He made a guest professor stay at Nottingham University, UK during spring/summer of 2018. His research interest is application of advanced control, optimization and artificial intelligence inspired techniques to provide innovative and effective solutions to emerging challenges in design, control and diagnostics of power electronics intensive electrical distributions systems and microgrids. He has authored and co-authored more than 330 technical publications (more than 150 of them are published in international journals, mostly in IEEE), 10 book chapters and a book in this field, as well as filed for several patents.

He serves as an Associate Editor in the IEEE TRANSACTIONS ON INDUSTRIAL ELECTRONICS, in IEEE TRANSACTIONS ON POWER ELECTRONICS, in IEEE Emerging and Selected Topics in Power Electronics and in IEEE Industrial Electronics Magazine. Prof. Dragičević is a recipient of the Končar prize for the best industrial PhD thesis in Croatia, a Robert Mayer Energy Conservation award, and he is a winner of an Alexander von Humboldt fellowship for experienced researchers.